

Petrogenesis of the ~2.77 Ga Monts de Cristal Complex, Gabon: Evidence for Direct Precipitation of Pt-arsenides from Basaltic Magma

W. D. Maier^{1*}, B. Rasmussen², I. R. Fletcher², B. Godel³, S. J. Barnes³, L. A. Fisher³, S. H. Yang⁴, H. Huhma⁵ and Y. Lahaye⁵

¹School of Earth and Ocean Sciences, Cardiff University, Park Place, Cardiff CF10 3AT, UK, ²Department of Applied Geology, Curtin University, Perth, WA 6102, Australia, ³CSIRO, Kensington, WA6152, Australia, ⁴Oulu Mining School, University of Oulu, 90014 Oulu, PO Box 8000, Finland and ⁵GTK (Geological Survey of Finland), Espoo 02151, PO Box 96, Finland

*Corresponding author. E-mail: MaierW@cardiff.ac.uk

Received April 11, 2014; Accepted June 16, 2015

ABSTRACT

The Monts de Cristal Complex of Gabon consists of several igneous bodies interpreted to be remnants of a tectonically dismembered, >100 km long and 1–3 km wide, ultramafic–mafic intrusion emplaced at 2765–2775 Ma. It is the most significant mafic–ultramafic layered complex yet identified on the Congo Craton. The complex consists largely of orthopyroxenite cumulates, with less abundant olivine–orthopyroxenite and norite, and rare harzburgite and dunite. Mineral compositions (Fo_{ol} 84, $Mg\#_{Opx}$ 85, An_{plag} 60–68, Cr/Fe chromite 1–1.45) and whole-rock data suggest that the parent magma was a low-Ti basalt containing approximately 10% MgO and 0.5% TiO₂. Trace element and Rb–Sr and Sm–Nd isotope data indicate the presence of an enriched component, possibly derived from crustal contamination of a magma generated in the sub-lithospheric mantle. Most rocks show a highly unusual pattern of strong Pt enrichment (10–150 ppb) at low concentrations of Pd (1–15 ppb), Au (1–2 ppb), Cu (1–20 ppm), and S (<500 ppm), suggesting that unlike in most other PGE-rich intrusions globally, platinum in the Monts de Cristal Complex is not hosted in magmatic sulfides. Synchrotron X-ray fluorescence mapping has revealed the location of buried small Pt particles, most of which are associated with As. We propose that this constitutes some of the strongest evidence yet in support of magmatic crystallization of a Pt–As phase from S-undersaturated magma.

Key words: Gabon; layered intrusion; platinum-group elements; Pt arsenide; synchrotron

INTRODUCTION

The Monts de Cristal (MdC) Complex, locally also referred to as the Kinguele Complex, is located in NW Gabon, some 70–150 km to the NE of Libreville, and ~50–100 km north of the Equator (Fig. 1a). It forms a tectonically dismembered intrusion, ~100 km in length and mostly ~1–3 km wide (Fig. 1b), constituting the largest mafic–ultramafic layered intrusion so far discovered on the Congo Craton. In terms of its inferred shape and the observed lithologies, it bears some resemblance to the platinum group element (PGE) mineralized Great Dyke

of Zimbabwe. Based in part on this analogy, several companies have conducted exploration for chromite seams and PGE reefs in the MdC Complex during recent decades. After initially obtaining promising exploration indicators, particularly elevated Pt concentrations along most of the strike of the complex, it was ultimately realized that the Pt is not associated with cumulus magmatic sulfide, in contrast to economic PGE reefs elsewhere. However, the strong enrichment of Pt relative to Pd in the MdC Complex is of considerable petrological significance, in that it constitutes the most convincing case yet identified

for direct precipitation of Pt phases from basaltic magma. In this study, we provide a description and compositional characterization of these unique Pt-enriched rocks and suggest a model for their formation.

REVIEW OF PREVIOUS WORK

The first account of mafic rocks in the MdC area was published by [Arsandaux \(1912\)](#), who reported the presence of ophitic gabbros associated with charnockite to the south of Kinguele. Noritic massifs were first indicated in the Libreville Est geological map of 1959 ([Aubague & Hausknecht, 1959](#)), but reconnaissance mapping of the intrusion began only in the 1980s when the Direction Générale des Mines et de la Géologie du Gabon, in collaboration with the French Bureau de Recherches Géologiques et Minières, carried out a regional mineral assessment comprising airborne geophysical surveys and stream geochemistry over an area of $\sim 100\,000\text{ km}^2$. This program identified Archaean granite–gneiss basement rocks containing banded iron formations and amphibolites as well as gabbro-noritic intrusive rocks. The presence of ultramafic intrusive rocks was first indicated in the 1:200 000 Kango geological sheet ([Kassa-Mombo *et al.*, 1988](#)). Mineral exploration activities initially focused on chromite, but no massive seams were found and the detrital chromite grains turned out to be too Fe- and Al-rich to be of economic interest ([Campiglio *et al.*, 1983](#)). Reconnaissance geochronological work indicated an age of $\sim 2.78\text{ Ga}$ ($2777 \pm 83\text{ Ma}$, Rb–Sr on whole-rocks; $2783 \pm 77\text{ Ma}$, Pb–Pb on whole-rocks; [Caen-Vachette *et al.*, 1988](#)).

In 2002, Southern Era Resources Limited started an exploration program for PGE in the MdC Complex, comprising mapping, comprehensive stream sediment sampling, and soil sampling. Significant Pt anomalies closely associated with all blocks of the intrusion were delineated and a large number of outcrop samples were collected for high-precision geochemistry and geochronology ([Maier, 2004](#)). The exploration licence was acquired by Lonmin in 2005, which carried out extensive soil sampling at KG1, KG1 extension and KG3, and remapped some of the bodies ([Fig. 1b](#); [Prendergast, 2009](#)). The company also drilled 15 diamond drill holes (13 holes at KG1 and two holes at KG3). In addition, a detailed magnetic-radiometric survey was conducted by Fugro Airborne Surveys in 2008.

ANALYTICAL METHODS

Whole-rock and mineral chemistry

Seventy-five samples were analysed for major and minor elements as well as a range of lithophile trace elements including Sr, Rb, Nb, Y, Zr, Ni, Cu, Zn, Co, Cr, Sc, V and rare earth elements (REE) using inductively coupled plasma mass spectrometry (ICP-MS) at Cardiff University, UK, after grinding to $<75\text{ }\mu\text{m}$ in agate ring and ball mills. The concentrations of the PGE were determined using ICP-MS after nickel sulfide fire assay

and tellurium co-precipitation, on 15 g aliquots. Full details of the analytical procedures used have been given by [McDonald & Viljoen \(2006\)](#). The analytical procedure was validated by frequent analysis of reagent blank samples, replicate samples and reference materials ([Supplementary Data Electronic Appendix 1](#); [supplementary data are available for downloading at <http://www.petrology.oxfordjournals.org>](#)). All the whole-rock data are reported in [Supplementary Data Electronic Appendix 2](#), and [average compositions of the rock types](#) are given in [Table 1](#). In addition to the outcrop samples, Lonmin analysed ~ 2000 samples from 13 drill cores for Pt, Pd and Au as well as selected major (Fe, Mg, Al, Ca), minor (Ti, Mn) and trace elements (Cr, Ni, Cu, Co, V, Zn, S, and Zr), at Genalysis, Johannesburg, using Pb-collection fire assay followed by mass spectrometry for Pt, Pd and Au, and ICP-MS for a range of other major and trace elements. The Pt contents and the Pt/Pd ratios from the commercial laboratory show good overlap with the ICP-MS PGE data, suggesting that the two methods have broadly similar accuracy ([Maier, 2009](#)).

In situ Sr isotope analyses of plagioclase were performed by laser ablation (LA)-ICP-MS using a Nu Plasma HR multi-collector (MC)-ICP-MS system and a Photon Machine Analyte G2 laser microprobe at the Geological Survey of Finland (GKT) in Espoo. Analytical details have been given by [Yang *et al.* \(2013\)](#), and the complete data are provided in [Supplementary Data Electronic Appendix 3](#).

Whole-rock Nd isotopes were also determined at GTK in Espoo. Analytical details have been given by [Huhma *et al.* \(2012\)](#); data for five samples are reported in [Supplementary Data Electronic Appendix 4](#).

The compositions of orthopyroxene, olivine, plagioclase and chromite were determined in five samples of (olivine)-orthopyroxenite, one sample of norite, and two samples of gabbro from the KG1 and KG3 blocks ([Supplementary Data Electronic Appendices 5–8](#)). The instrument used was a JEOL JXA-8200 electron microprobe at the University of Oulu, operated at an accelerating voltage of 15 kV and a beam current of 30 nA. The accuracy of analyses was monitored using reference material of similar composition. The reproducibility varied by less than 2%.

Synchrotron X-ray fluorescence microscopy

X-ray fluorescence microscopy (XFM) using synchrotron radiation is a highly effective technique for locating ultra-trace high-Z components, owing to the effective penetration of the X-ray beam and the fluorescent target X-rays through sample volume. A protocol has been developed for searching for micron-scale precious metal (Au, PGE) enriched grains within geological materials ([Ryan *et al.*, 2014](#)). XFM was performed on the XFM beamline at the Australian Synchrotron in Melbourne ([Paterson *et al.*, 2011](#)) using the Kirkpatrick Baez mirror microprobe end-station. This provides a monochromatic $2\text{ }\mu\text{m}$ beam spot size for energies in the range 4–20 keV. Equipped with the Maia 384 detector

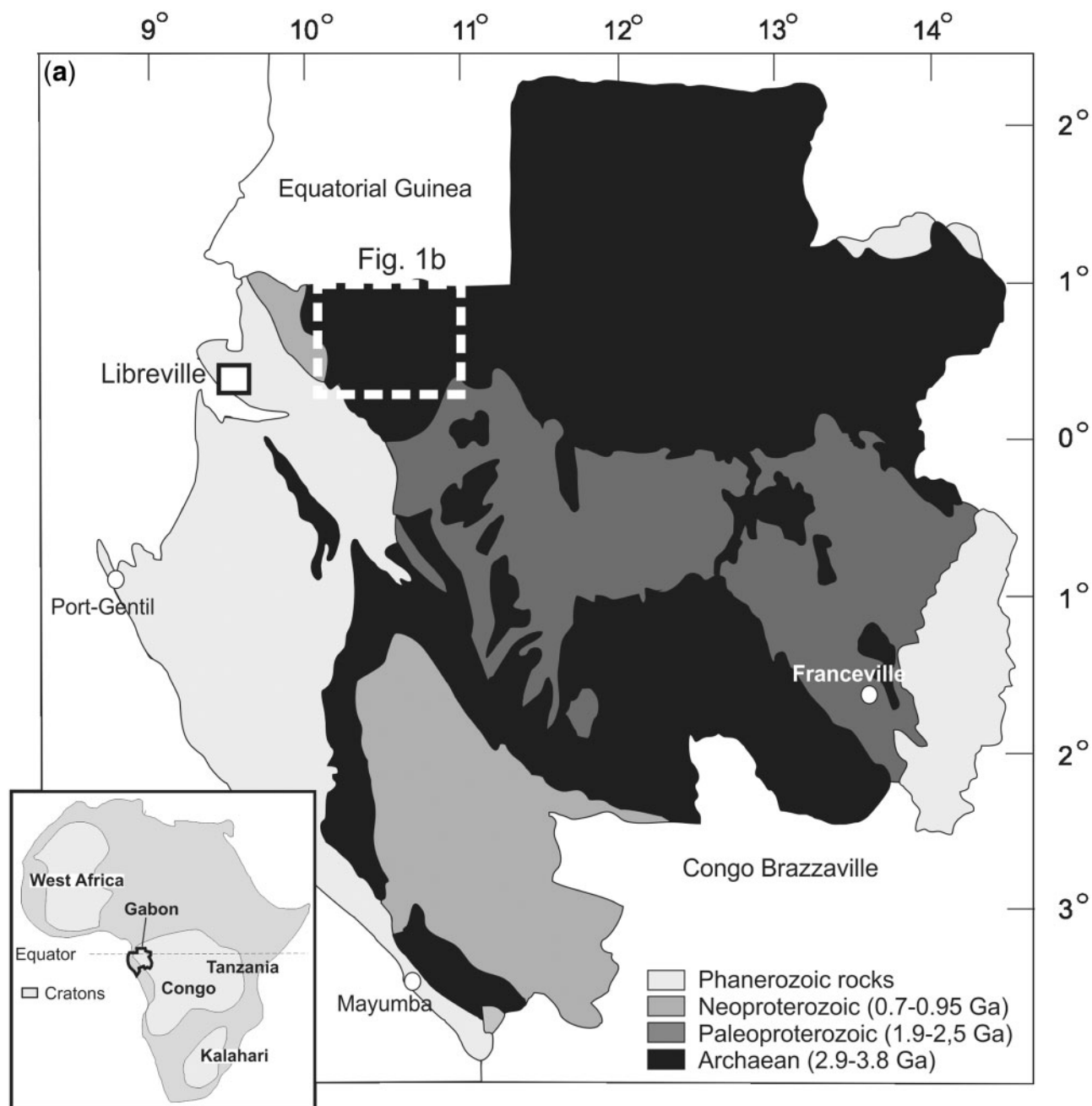


Fig. 1. (a) Geological map of Gabon [modified after [Chevalier et al. \(2002\)](#)]. Dashed rectangle shows the area enlarged in (b). (b) Geological map of the Monts de Cristal Complex and its host rocks. Red line denotes the outline of the Monts de Cristal National Park. KG1–4 are blocks of the complex; shaded areas with pink outline represent exploration focus areas. BIF, banded iron formation; TTG, tonalite–trondhjemite–granodiorite.

array, the XFM beamline can acquire images at $2\ \mu\text{m}$ resolution over areas of several square centimetres ([Kirkham et al., 2010](#); [Ryan et al., 2010a](#)) with count rates of $\sim 4\text{--}10\ \text{M s}^{-1}$ and energy resolution of 300–400 eV. In this study, large area element maps were collected on $100\ \mu\text{m}$ thickness polished thin sections backed by 1 mm quartz glass slides with a beam energy of 18.5 keV, spot size of $2\ \mu\text{m}$ and a dwell time per pixel of 0.97 ms to locate areas where Pt-rich inclusions were observed. For each sub-area identified additional maps were collected with longer dwell time (15–26 ms per pixel) to enhance

the signal-to-noise ratio and improve further quantification. Each dataset was analysed using the GeoPIXE software suite, which uses a fundamental parameters approach, with spectral deconvolution and imaging using the Dynamic Analysis method ([Ryan, 2000](#); [Ryan et al., 2010c](#)) and a detailed model of Maia detector array efficiency ([Ryan et al., 2010b](#)). Data were fitted using a yield file, which calculates the effects of X-ray absorption by the given matrix or mineral phase ([Ryan, 2000](#)). Element maps were produced after spectra were fitted and a dynamic analysis matrix file was produced.

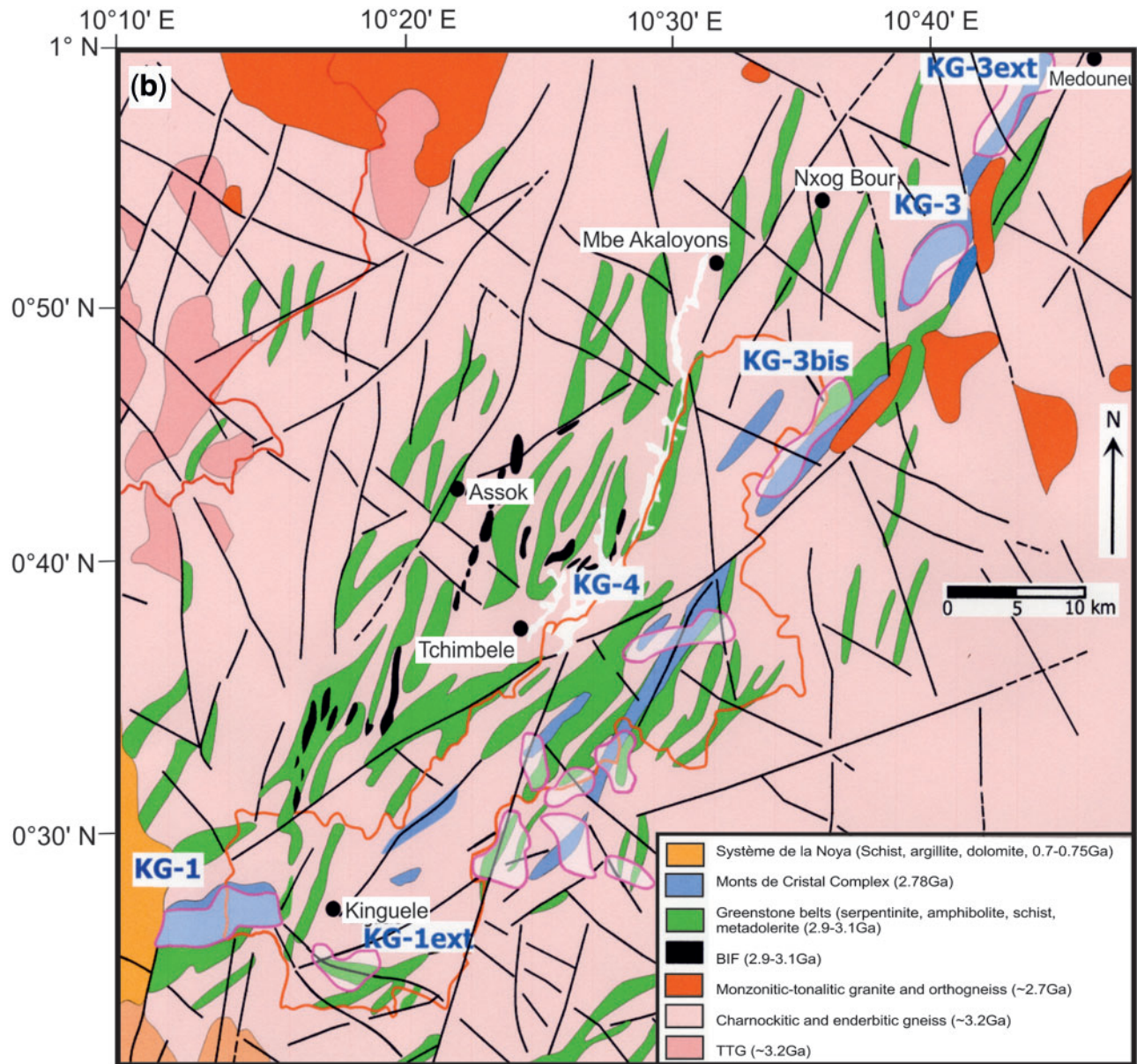


Fig. 1. Continued

Platinum abundance was measured using the $L\alpha$ line. These maps were then interrogated to confirm the presence of Pt and identify associated elements and phases. It must be noted that this method samples potentially the entire 100 μm thickness of the section, and thus Pt may be sitting on a buried grain boundary even if it appears to be within a grain. The true nature of the grain location is difficult to resolve without milling down to the grain, but it is possible to further interrogate the spectra to gain a rough quantification of probable depth in the sample to assist with this. The correct identification of Pt has been confirmed by matching XFM maps collected using this method with Pt phases identified at the sample surface by optical microscopy in sulfide ore samples (Barnes *et al.*, 2011), although as yet we have not identified any optically visible Pt phases in the MdC

samples. Identification of Pt phases in the samples has been confirmed by high-resolution PIXE imaging (Barnes *et al.*, in preparation).

Geochronology

Examination of orthopyroxenite samples Px12, Px39 and 1290 by scanning electron microscope revealed the presence of four minerals that can be used as U–Pb geochronometers: baddeleyite, zircon, zirconolite and monazite (Supplementary Data Electronic Appendix 9). However, the zircon grains appeared to have been affected by radiation damage and zirconolite was largely destroyed by secondary alteration, rendering both unsuitable for dating. Baddeleyite and monazite were viable for ion microprobe geochronology but the small

Table 1: Whole-rock compositions of Monts de Cristal rock types (average compositions)

n:	Orthopyroxenite		Ol-pyroxenite		Norite		Gabbro		Pegmatoid	Amphibolite		Granite	
	34	2 σ	24	2 σ	14	2 σ	2	2 σ	1	4	2 σ	2	2 σ
SiO ₂ (wt %)	52.84	2.41	50.72	4.40	51.04	2.24	47.22	0.80	49.56	47.98	0.77	72.02	13.47
TiO ₂	0.17	0.10	0.14	0.11	0.21	0.15	0.74	0.07	0.17	1.40	0.48	0.31	0.35
Al ₂ O ₃	5.02	3.68	4.08	2.58	10.73	5.45	15.36	1.05	1.42	13.74	1.18	15.40	3.32
Fe ₂ O ₃	0.27	0.29	0.20	0.31	0.92	0.67	1.19	0.04	0.00	1.54	0.13	0.27	0.38
FeO	9.34	1.01	10.20	1.61	7.92	4.29	9.64	0.33	21.57	12.49	1.05	2.15	3.05
MnO	0.19	0.03	0.19	0.02	0.17	0.07	0.19	0.00	0.36	0.23	0.04	0.05	0.08
MgO	25.68	5.05	27.84	4.52	17.49	3.45	8.73	0.59	18.48	5.96	1.38	1.06	1.46
CaO	3.66	2.01	2.98	1.63	7.35	2.62	12.36	0.04	4.82	9.94	1.79	2.89	3.52
Na ₂ O	0.70	0.73	0.41	0.50	1.53	0.99	1.96	0.62	0.11	3.13	2.34	4.01	1.83
K ₂ O	0.09	0.14	0.08	0.18	0.30	0.61	0.14	0.22	0.07	0.43	0.36	1.71	1.93
P ₂ O ₅	0.02	0.03	0.01	0.02	0.02	0.02	0.06	0.02	0.02	0.15	0.07	0.11	0.20
Cr ₂ O ₃	0.44	0.14	0.54	0.11	0.28	0.11	0.06	0.01	0.11	0.02	0.02	0.01	0.01
NiO	0.10	0.03	0.15	0.04	0.08	0.04	0.02	0.00	0.05	0.01	0.01	0.00	0.00
LOI	0.25	0.62	1.46	2.42	0.73	1.62	0.31	0.23	0.46	0.56	0.39	0.56	0.03
Total	98.76	1.75	99.00	1.02	98.77	1.39	97.99	0.03	97.19	97.58	0.75	100.54	1.17
Mg#	0.83	0.03	0.83	0.03	0.80	0.07	0.62	0.01	0.61	0.46	0.07	0.47	0.01
Sc (ppm)	26	4	23	4	25	10	36	2	41	43	6	4	3
V	134	28	126	25	128	51	224	12	124	348	46	39	76
Cr	2987	956	3686	783	1907	772	439	64	755	149	124	63	52
Co	92	15	112	29	74	17	58	3	91	64	6	9	8
Cu	18	14	17	15	28	26	108	6	8	138	50	19	10
S	62	62	65	46	111	236	351	10	166	1135	141	39	16
Sr	43	54	29	36	130	91	108	8	-3	106	16	391	742
Y	4.6	2.9	3.7	3.1	6.0	3	17.5	1.8	6.7	34.8	10.0	11.1	6.0
Zr	17.7	18.8	13.4	17.9	22.2	22.7	45.3	9.1	5.5	115.2	48.9	193.7	19.1
Ni	794	249	1205	314	630	281	196	6	385	95	42	33	23
Zn	40	7	39	5	40	10	47	3	62	61	6	87	95
Ga	6.66	2.91	5.80	2.55	10.56	2.91	16.29	0.30	4.02	20.28	2.44	19.36	3.13
Rb	4.11	5.11	3.17	6.52	10.17	22.44	2.72	0.39	0.98	11.26	14.62	56.88	76.48
Nb	0.77	0.93	0.58	0.79	0.98	0.93	2.21	0.24	0.14	5.24	2.17	5.89	3.71
Ba	68	56	52	72	154	187	62	1	36	142	65	852	38
La	2.38	2.69	1.79	2.79	3.88	4.95	3.65	0.66	0.32	9.68	5.43	37.80	54.13
Ce	4.99	5.54	3.82	5.07	7.65	7.92	8.54	1.36	0.86	21.39	8.06	77.76	120.28
Pr	0.59	0.65	0.45	0.57	0.90	0.93	1.27	0.21	0.19	2.99	1.11	8.01	10.91
Nd	2.15	2.32	1.62	2.06	3.31	3.39	5.84	0.77	0.93	13.13	4.89	25.83	29.91
Sm	0.47	0.48	0.35	0.43	0.72	0.71	1.82	0.12	0.35	3.92	1.49	4.36	4.24
Eu	0.15	0.13	0.12	0.13	0.29	0.19	0.70	0.07	0.10	1.24	0.43	0.80	0.45
Gd	0.52	0.49	0.39	0.45	0.79	0.73	2.34	0.12	0.50	4.75	1.59	3.32	3.24
Tb	0.09	0.08	0.07	0.08	0.14	0.12	0.44	0.04	0.11	0.88	0.28	0.41	0.36
Dy	0.64	0.48	0.50	0.49	0.90	0.67	2.80	0.20	0.81	5.51	1.77	1.88	1.35
Ho	0.13	0.09	0.10	0.09	0.18	0.12	0.55	0.03	0.17	1.07	0.33	0.31	0.21
Er	0.43	0.29	0.34	0.29	0.56	0.35	1.68	0.10	0.60	3.33	1.05	0.89	0.48
Tm	0.07	0.04	0.06	0.05	0.09	0.05	0.27	0.03	0.11	0.53	0.17	0.13	0.06
Yb	0.47	0.26	0.39	0.28	0.57	0.30	1.66	0.12	0.71	3.28	1.02	0.73	0.29
Lu	0.08	0.04	0.07	0.04	0.09	0.05	0.27	0.01	0.12	0.52	0.15	0.12	0.05
Hf	0.43	0.47	0.33	0.46	0.58	0.59	1.22	0.18	0.18	2.99	1.26	4.81	0.72
Ta	0.06	0.09	0.05	0.07	0.08	0.07	0.15	0.04	0.01	0.37	0.16	0.46	1.03
Pb	10.29	12.19	11.51	13.30	9.56	13.87	3.67	0.47	17.07	8.01	13.83	25.31	11.26
Th	0.87	1.23	0.65	1.04	1.17	1.37	0.57	0.14	0.04	2.49	1.39	25.84	69.05
U	0.25	0.36	0.18	0.33	0.31	0.32	0.14	0.05	0.00	0.72	0.47	7.04	19.18
Os (ppb)	0.51	0.50	0.47	0.37	0.27	0.32	0.14	0.04	0.04	0.04	0.04	0.09	0.10
Ir	0.85	0.92	0.99	1.34	0.45	0.51	0.15	0.06	0.07	0.07	0.09	0.10	0.16
Ru	3.57	2.75	5.74	2.39	2.35	1.99	0.59	0.04	0.34	0.28	0.19	0.26	0.13
Rh	3.19	2.43	2.92	1.56	1.62	0.95	0.79	0.38	0.09	0.12	0.05	0.17	0.16
Pt	30.8	38.0	19.5	13.1	11.5	10.4	6.5	1.1	0.9	2.2	4.7	1.4	1.7
Pd	4.77	3.68	4.28	5.79	8.49	11.47	8.86	1.22	0.67	0.81	0.70	0.62	0.24
Au	1.20	1.71	0.81	1.23	1.33	1.57	1.93	0.01	0.84	0.54	0.47	0.39	0.11

Note: FeO and Fe₂O₃ contents have been calculated assuming that Fe in the cumulus minerals is in the form of FeO and FeO/Fe₂O₃ ratio in the trapped liquid is 9:1.

size and limited number of grains constrain the data quality. Crystals of both minerals >10 μm in size were drilled from polished thin sections in ~3 mm platelets and mounted in 25 mm resin disks for sensitive high-resolution ion microprobe (SHRIMP) analysis.

Baddeleyite was analysed using an ~0.15 nA O₂⁻ primary ion beam focused on a <10 μm spot. A chip of Phalaborwa (2060 Ma) baddeleyite was mounted with the samples for Pb/U calibration and as a monitor of Pb isotope data quality. Monazite analyses used an

$\sim 10\ \mu\text{m}$, 0.25 nA primary ion beam. Monazite reference samples (French, PD-95, z2234 and QMa28-1) were held in a separate mount that was cleaned and Au-coated with the sample mount. Baddeleyite data acquisition and reduction followed the procedures of [Wingate *et al.* \(1998\)](#). Monazite analytical procedures were those of [Fletcher *et al.* \(2010\)](#). Primary data reduction was performed using Squid-2 software ([Ludwig, 2009](#)), using 'spot average' data for all ratios. Corrections to monazite data for matrix effects in Pb/U and Pb/Th and a small correction for instrumental mass fractionation were applied.

STRUCTURE AND LITHOLOGIES

The MdC Complex is largely hosted within Archaean basement rocks comprising granite–gneiss and greenstones. The basal contacts of the intrusions dip steeply towards the centres of the intrusive blocks ($\sim 80^\circ$) and are defined by aphanitic margins, grading inwards to medium-grained norite, orthopyroxenite and, less abundantly, harzburgite and dunite ([Edou-Minko *et al.*, 2002](#)). In addition, the Southern Era and Lonmin exploration programs discovered isolated anorthosite layers and several occurrences of ophitic gabbro, the latter located near the margins of the KG1 and KG3 blocks. All mafic–ultramafic rocks are generally poorly layered and lack distinct differentiation cycles. The norites appear to form lenses within the orthopyroxenites rather than distinct, laterally persistent, layers. In addition, norites appear to be relatively common towards the basal contact of the intrusions; for example, at KG3 (drill core MPD-015) and at KG1 (drill cores MPO-03 and 04). Xenoliths of the country rocks, consisting mainly of feldspar-rich amphibolite as well as less abundant felsic fragments, have been intersected in several boreholes at the KG1 intrusive block.

The most comprehensive information on the geology of the complex is available from KG1, where an extensive soil geochemical program was conducted ([Prendergast, 2009](#)). The locations of the grab samples analysed by us, and of some of the boreholes drilled by Lonmin in 2007–2008, are indicated in [Fig. 2](#). The KG1 mafic–ultramafic body measures $\sim 8\ \text{km}$ by $2\ \text{km}$ and appears to consist of two distinct blocks ([Prendergast, 2009](#); [Fig. 2](#)). In the west and north, the intrusion is hosted by felsic gneisses and mafic schists interpreted to represent a granite–gneiss–greenstone terrane. Tonalitic to granodioritic granite gneiss containing intercalations of quartzite, amphibolite and ultramafic slivers occurs to the south and east of the body. Proterozoic clastic and chemical sedimentary rocks occur to the west of an inferred NNE–SSW-trending fault, 1–2 km west of KG1. Most contacts of the intrusion with its host rocks are tectonic ([Prendergast, 2009](#)), but the intrusive basal contact of the body has been intersected by drill cores MPD-03 and 04 ([Fig. 2](#)). This intrusive contact consists of a 1–2 m aphanitic rock interpreted as a chilled margin that grades to orthopyroxenite ([Supplementary Data Electronic Appendix 10](#)). Based on the concordance of the strike of layering with

the NW flank of the intrusion, [Prendergast \(2009\)](#) proposed that the intrusive contact strikes SW–NE and dips at $\sim 60^\circ$ to the SE, and that the total stratigraphic thickness is $\sim 1700\ \text{m}$. The dip of layering in most of the remainder of the complex remains unclear, owing to weathering and paucity of layering.

The rocks of the KG1 block are mainly massive orthopyroxenites. Norites appear to be relatively abundant along the south–central margin, whereas olivine pyroxenite and occasional harzburgite predominantly occur in the east, consistent with elevated Ni values in soil sediment surveys. In drill core MPD-03 there is an $\sim 400\ \text{m}$ basal reversal expressed by a downward decrease in grain size together with an increase in modal plagioclase and biotite, relatively prevalent orthocumulate textures, several noritic intervals, occasional acicular textures, and enclaves of felsic melt rock. In another drill core (MPD-01), relatively fine-grained orthopyroxenite overlying the floor contains xenoliths of amphibolite. All segments of the MdC intrusion are cut by abundant amphibolized plagioclase–clinopyroxene–phyric dolerites of unknown age.

PETROGRAPHY

The ultramafic rocks are mostly heteradcumulates or mesocumulates with between ~ 5 and 15% intercumulus material ([Fig. 3a–c](#)). Orthocumulates are less abundant and are mainly confined to the stratigraphically lower portions of the intrusion. Considering the Archean age of the complex, most rocks are remarkably unaltered. Minor to moderate serpentinization and chloritization is observed, predominantly in the olivine-bearing lithologies. Orthopyroxene is mostly up to 2 mm in size, commonly of euhedral or subhedral habit ([Fig. 3b and c](#)), and aligned subparallel to the layering. Olivine forms anhedral grains up to 4 mm in width that can be moderately altered to serpentine and magnetite. Plagioclase occurs as either intercumulus, poikilitic or, in places, cumulus grains. In the orthopyroxenites, chromite tends to be rare, forming occasional clusters and chains of very small ($< 0.01\ \text{mm}$) euhedral and subhedral crystals included in orthopyroxene ([Fig. 3d and e](#)). Chromite is slightly more abundant in olivine pyroxenites, where grains tend to be larger (up to 0.1 mm) and may occur within, or interstitial to, orthopyroxene. Clinopyroxene is relatively rare as an interstitial phase (mostly < 1 –2 modal %), but commonly forms exsolution lamellae and blebs in orthopyroxene. Phlogopite is a common accessory phase and may constitute up to 2 modal % in some samples. Hornblende, tremolite and actinolite are accessory phases, largely related to alteration. Sulfides form small grain aggregates up to about $20\ \mu\text{m}$ in size mostly located on orthopyroxene grain boundaries and consist of pyrrhotite, pentlandite and chalcopyrite. Notably, many orthopyroxenes are distinctly zoned showing dark rims ([Fig. 3c](#)). Synchrotron X-ray fluorescence mapping has shown the rims to be Ti enriched. The absence of residual phases such as

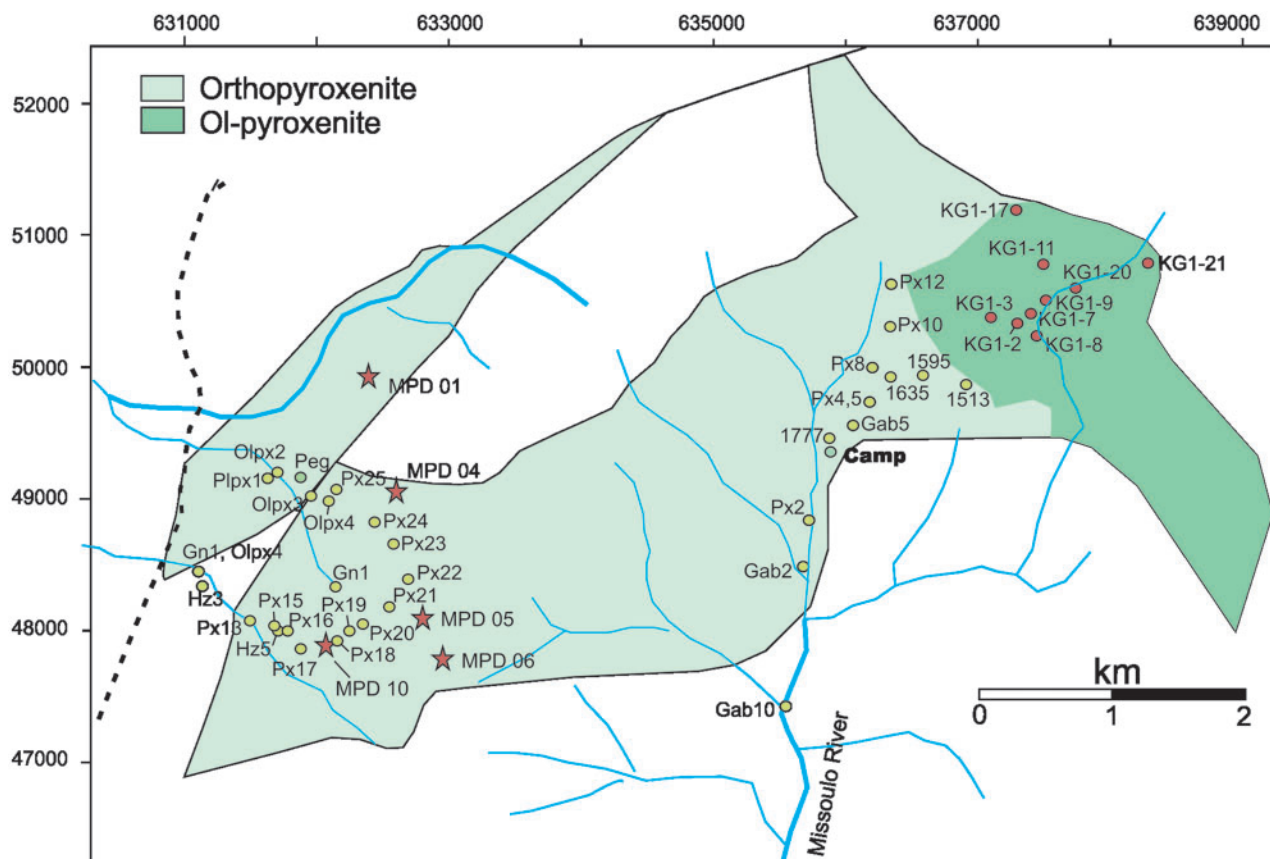


Fig. 2. Geological map of the KG1 body, showing sampling localities and drill-core sites (denoted by stars) [modified after Prendergast (2009)]. Dashed line indicates a road.

apatite, amphibole or K-feldspar implies that the last few per cent of trapped liquid was completely expelled from the rock during heteradcumulate formation, at least at the scale of a thin section.

Norites consist mainly of subhedral orthopyroxene and intercumulus or cumulus plagioclase. The latter forms tabular subhedral crystals up to 4 mm in length (Fig. 3f). Clinopyroxene is intercumulus and phlogopite, quartz and alkali feldspar are accessory phases. Chromite is rare, occasionally occurring as clusters of very small grains included in orthopyroxene, similar to the orthopyroxenites. Based on the above observations, the crystallization sequence of the exposed portion of the Monts de Cristal intrusion is $ol + cr - opx - opx + pl - opx + pl + cpx$.

Gabbros are represented by just two samples, one from KG3 (sample Dy18), and the other from KG1 west (sample Hz3). The rocks have a medium-grained ophitic texture, containing tabular, elongated plagioclase (up to 1 mm long) and anhedral or subhedral clinopyroxene (up to 2 mm) (Fig. 3g and h). Olivine is a minor phase, forming mostly relatively small (<1 mm) anhedral crystals, but occasionally occurs as larger grains up to 1 cm across. Magnetite forms anhedral aggregates reaching up to 1–5 modal %. Sulfides comprise mainly pyrrhotite and chalcopyrite that form very small trace phases.

The amphibolites are fine- to medium-grained rocks. Plagioclase forms subhedral tabular crystals up to 2 mm long and <1 mm wide. Amphibole grains tend to be anhedral or, in some cases, subhedral, forming pseudomorphs after pyroxene. Some samples have granular textures and are finer grained, suggesting metamorphic recrystallization.

MINERAL CHEMISTRY

In general, the analysed MdC samples show relatively limited mineral compositional variation compared with other layered intrusions. Olivine is mostly 75–84 Fo with 2400–3600 ppm Ni, with one sample having 4400 ppm Ni. These Ni contents are higher than those of olivines with equivalent Fo contents in most other layered intrusions (Fig. 4). Orthopyroxene has Mg# 0.78–0.85, 200–1000 ppm Ni, 0.4–0.7% Cr_2O_3 , and up to 2% Al_2O_3 . Cumulus plagioclase is An 67, whereas intercumulus plagioclase is An 60–68. Chromite contains around 40% Cr_2O_3 , and has Cr/Fe of ~ 1 –1.4. Norites have approximately similar mineral compositions to the orthopyroxenites.

Two samples of fine-grained ophitic gabbro from the margins of the intrusion contain slightly less magnesian clinopyroxene (Mg# 0.77–0.8) than the orthopyroxenites and norites. Plagioclase (An 63–67) is of similar



Fig. 3. Photomicrographs of Monts de Cristal rocks. (a) Olivine pyroxenite showing olivine inclusions in orthopyroxene. Sample Olpx21. (b) Orthopyroxene adcumulate, sample Px21. (c) Orthopyroxenite mesocumulate. Zoning is indicated by dark coronas along rims of grains. Sample Px18. (d) Chromite clusters within orthopyroxene of orthopyroxenite adcumulate. Sample Px21. (e) Chromite clusters within altered inclusion in orthopyroxene. Sample Px21. (f) Norite, showing euhedral and subhedral orthopyroxene and cumulus and intercumulus plagioclase. Sample Px16. (g) Olivine gabbro, showing intercumulus olivine and clinopyroxene as well as acicular plagioclase crystals. Sample Dy18. (h) Olivine gabbro, showing large euhedral clinopyroxene oikocryst containing plagioclase chadacrysts. Sample Dy18. Length of scale bar in each panel represents 1 mm.

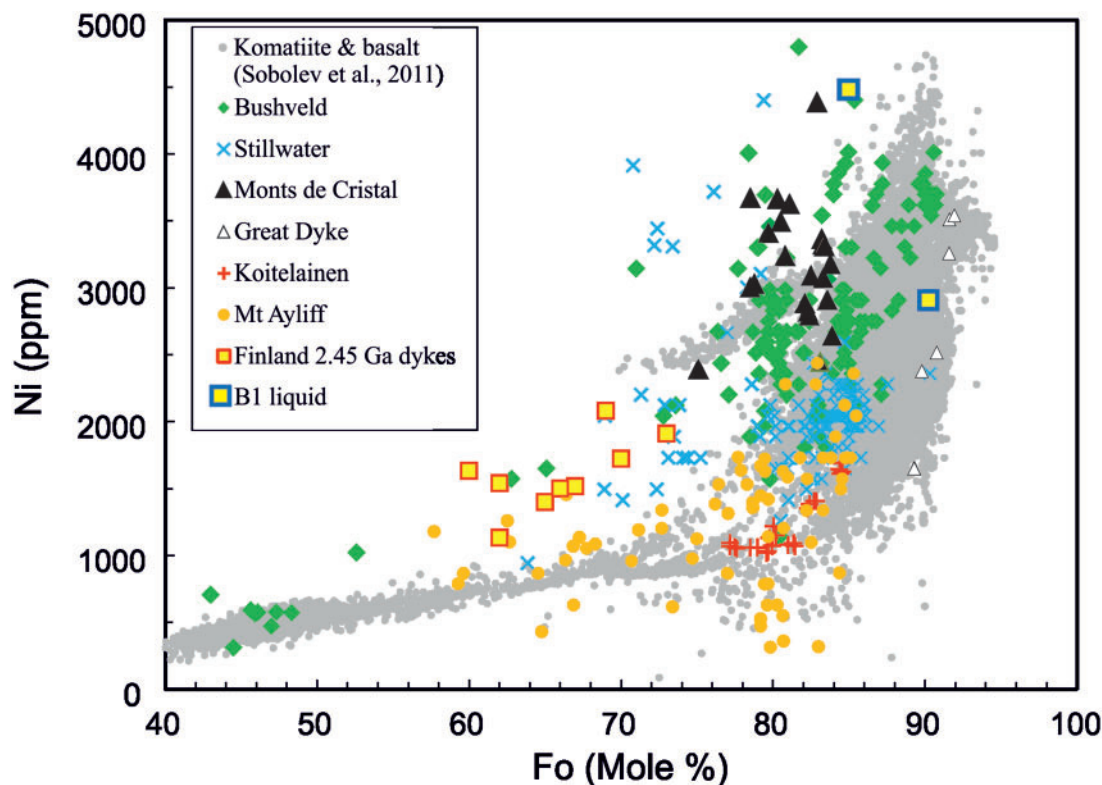


Fig. 4. Variation of Fo and Ni contents of olivine in a number of layered intrusions. The Monts de Cristal olivines have relatively high Ni contents compared with other intrusions with comparable Fo contents. Bushveld data are from Teigler & Eales (1996), Maier & Eales (1997) and Wilson (2012), Great Dyke data are from A. H. Wilson (personal communication, 2012), Koitelainen data are from E. Hanski (unpublished data; personal communication, 2013), Stillwater data are from Raedeke (1982) and Barnes & Naldrett (1986), Mt Ayliff data are from Lightfoot & Naldrett (1983) and Lightfoot *et al.* (1984), and Finnish dykes are the unpublished data of Fangfang Guo. Data for global komatiites and basalts are from Sobolev *et al.* (2011).

composition to that in the norites, but olivine in the gabbros is significantly more iron-rich (Fo 57–58) than in the other lithologies.

WHOLE-ROCK CHEMISTRY

Lithophile elements

Concentrations of Al_2O_3 , TiO_2 , Cr, and Ni are plotted vs MgO in Fig. 5a–d. The MdC orthopyroxenites and norites have between 15 and 32% MgO, whereas the ophitic gabbros have between 8.5 and 9% MgO. The concentrations of the major and minor elements are mainly controlled by the modal proportions of orthopyroxene, olivine, and plagioclase. Using the lever rule it is estimated that the proportion of olivine to orthopyroxene may be up to ~20%, consistent with petrographic data. The composition of the trapped melt cannot be well constrained, except for TiO_2 , where a best-fit line through the ultramafic rocks indicates TiO_2 levels in the trapped melt of around 0.5 wt %. REE patterns of most samples are fractionated (Supplementary Data Electronic Appendix 11), showing relative enrichment in light REE (LREE) over heavy REE (HREE), but $\text{Gd}/\text{Lu}_N < 1$. Only a few samples show slight positive or negative Eu anomalies. Incompatible trace element patterns show marked enrichment in large ion lithophile

elements (LILE), positive Th anomalies, and negative anomalies in Nb–Ta and P (Fig. 6).

Trace element contents in the two gabbro samples are more than five times those in the orthopyroxenites and norites. Together with their ophitic texture, this suggests that the samples may approach liquid compositions, either chilled against the margin of the intrusion or emplaced as dykes or sills. The rocks have 47–48% SiO_2 , 8.5% MgO, 12% Fe_2O_3 , 15% Al_2O_3 , 0.7–0.8% TiO_2 , 2% Na_2O and 0.1–0.2% K_2O (Table 1). They can thus be classified as Al-tholeiites. The multi-element patterns of the gabbros are much flatter and less fractionated than those of the orthopyroxenites and norites (Fig. 6). The two samples analysed have remarkably similar trace element patterns, considering that they were collected from two different intrusive blocks located >50 km apart. The patterns show only subtle negative Nb–Ta anomalies, reminiscent of many Archean basalts (Barnes *et al.*, 2012). Zirconium contents of the gabbros are ~50 ppm, in the range of Yilgarn low-Ti basalts (Barnes *et al.*, 2012), as are Cr and Ni contents (~400 ppm and 200 ppm, respectively).

The amphibolite dykes also have relatively flat trace element patterns (Fig. 6h). The concentrations of most incompatible trace elements are significantly elevated relative to the orthopyroxenites and norites, by an order

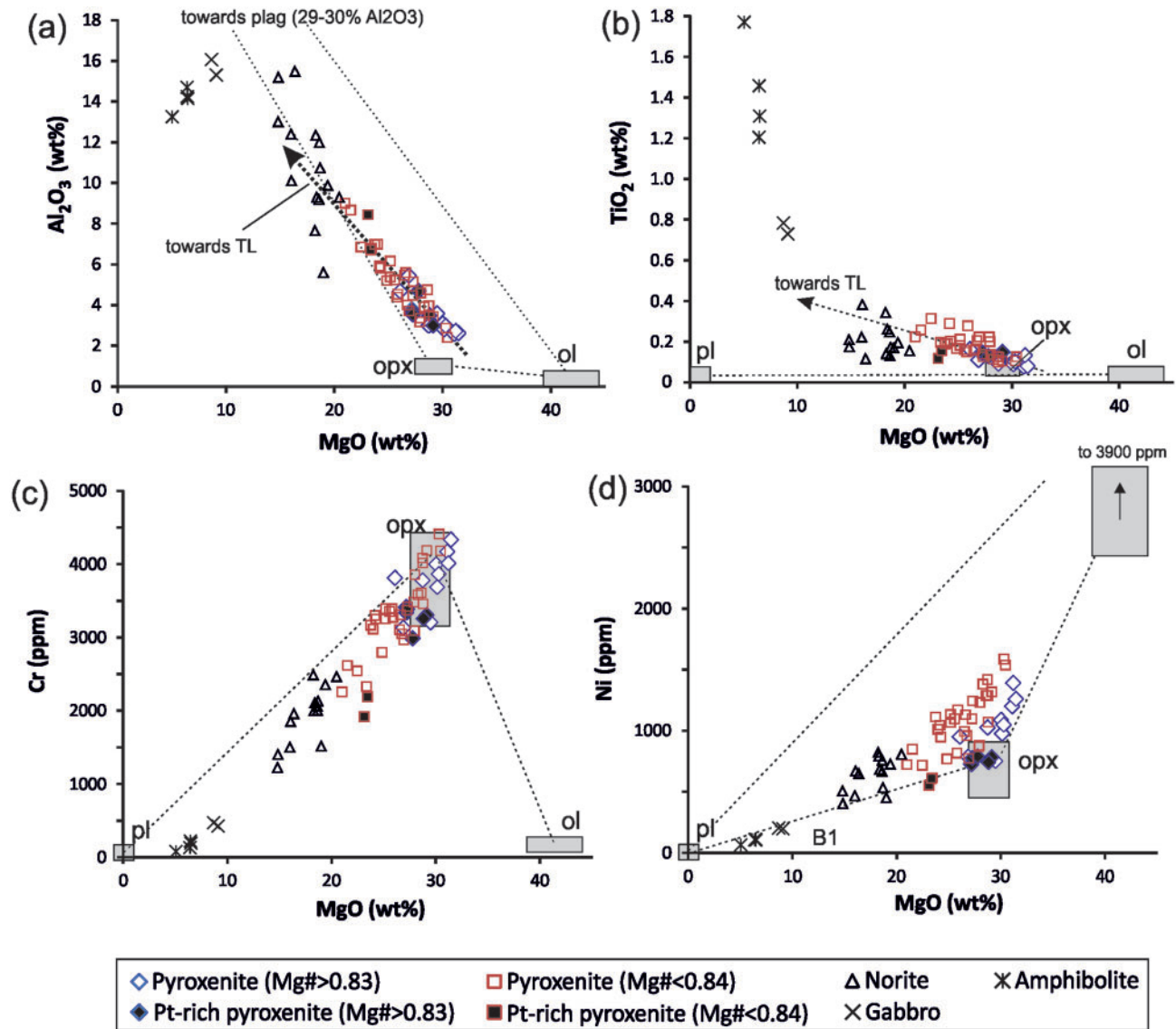


Fig. 5. Whole-rock variation of (a) Al_2O_3 , (b) TiO_2 , (c) Cr, and (d) Ni vs MgO wt %. Dotted arrows represent best-fit lines through orthopyroxenites. Boxes linked by tie-lines indicate compositional ranges in analysed minerals. TL indicates trapped liquid.

of magnitude. This is consistent with the amphibolites representing original liquid compositions. The shape of the multi-element patterns is broadly similar to those of the gabbros, except that the amphibolites have strong negative Sr anomalies and are relatively more enriched in LILE. Additionally, the amphibolites have markedly higher total incompatible element concentrations than the gabbros.

Sulphur and chalcophile elements

The sulphur contents of the MdC cumulates are mostly <100 ppm, consistent with the paucity of sulphides in thin section. Sulphur shows a weak positive correlation with TiO_2 (Fig. 7), suggesting that it behaved as an incompatible element during magma crystallization. We can place some constraints on the S content of the parent magma by means of the lever rule. The composition of the trapped melt can be estimated by a best-fit line

through the whole-rock compositions of the least evolved orthopyroxenites. Assuming a TiO_2 content of ~0.4–0.5% for the liquid, as indicated by TiO_2 –MgO relationships (Fig. 5b), the S content of the magma is between 100 and 300 ppm. As the S solubility of basaltic magmas at crustal pressures is of the order of 1000–2000 ppm (Mavrogenes & O'Neill, 1999), the MdC magma is probably strongly S-undersaturated.

Copper contents of the MdC orthopyroxenites and ol-pyroxenites are mostly between 5 and 40 ppm (Supplementary Data Electronic Appendix 12), showing a positive correlation with TiO_2 . This indicates that Cu behaved as an incompatible element during magmatic differentiation, that the initial liquid (at 0.4–0.5% TiO_2) contained ~50–60 ppm Cu, and that the magma did not equilibrate with a sulphide melt.

For the noble metals, two datasets are available; one is based on 75 outcrop samples collected during the

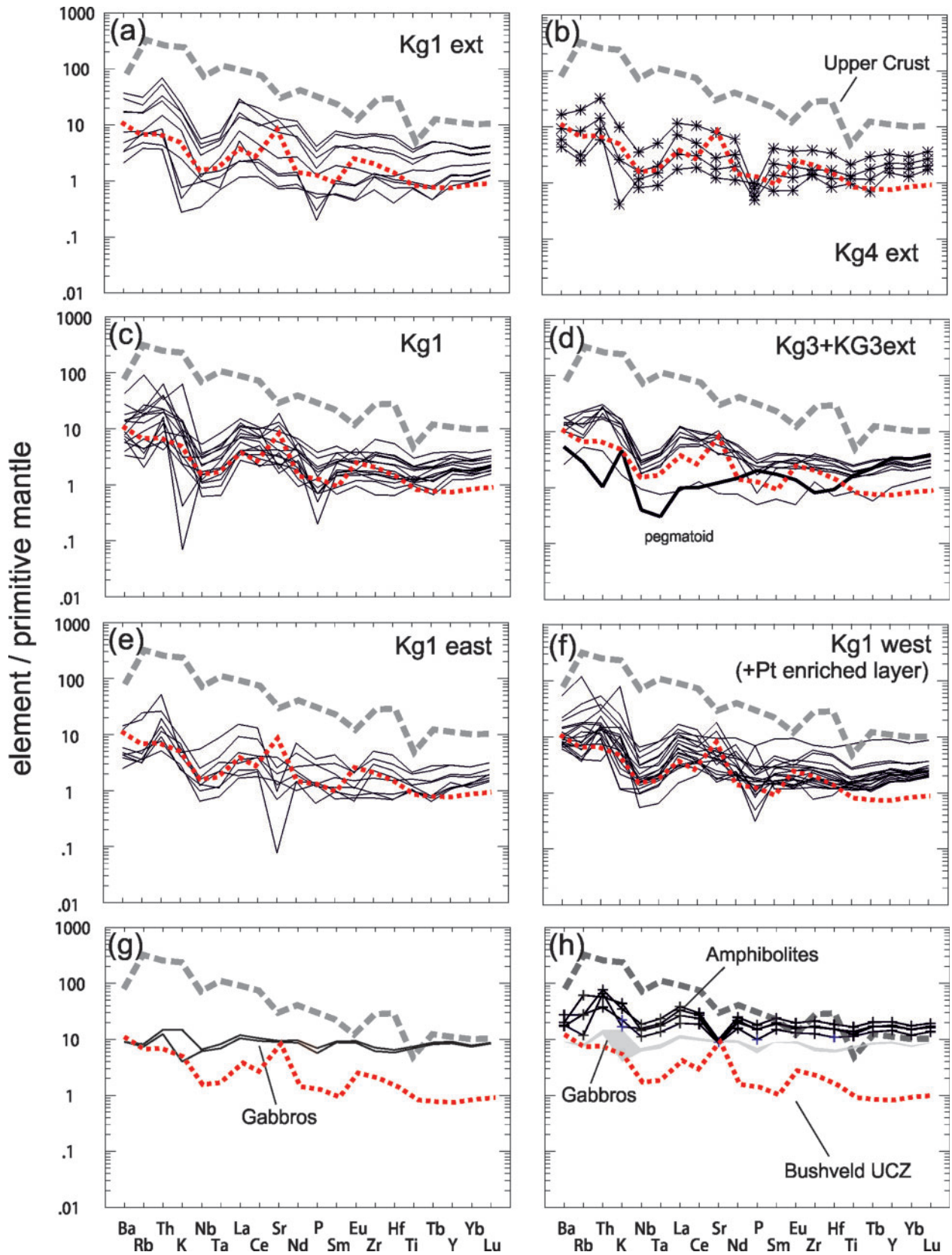


Fig. 6. Primitive mantle normalized trace element patterns of the MdC Complex. Data for Bushveld Upper Critical Zone (UCZ) are from [Maier et al. \(2013\)](#), and average upper crust is from [Rudnick & Fountain \(1995\)](#). Normalization factors from [McDonough & Sun \(1995\)](#).

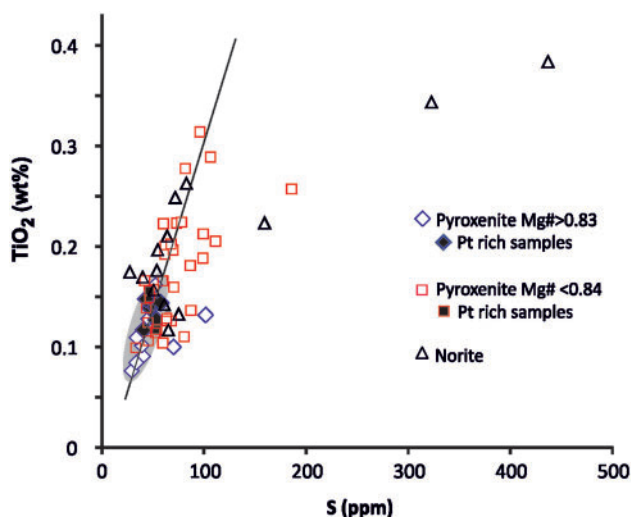


Fig. 7. Variation of TiO_2 (wt %) vs S (ppm) in MdC bulk-rocks. Regression line drawn through primitive orthopyroxenites (grey field, with exception of two samples) passes through the origin and suggests ~ 100 – 150 ppm S in the putative trapped liquid at 0.4–0.5% TiO_2 .

2004 field season (Fig. 8), whereas the other is based on several thousand drill-core samples analysed during 2007–2008 (Figs 9 and 10, and Supplementary Data Electronic Appendix 13). The outcrop samples have up to 70 ppb Pt, but mostly < 20 ppb Pd, < 2 ppb Au, < 6 ppb Rh, < 9 ppb Ru, and < 2 ppb Ir. The PGE contents in the drill cores cover a wider range extending to higher concentrations. The orthopyroxenites contain up to ~ 150 ppb Pt, 25 ppb Pd, 4 ppb Ir, 9 ppb Ru, 6 ppb Rh, and 3 ppb Au. With the exception of Pd and Au, the norites tend to have lower PGE contents than the orthopyroxenites; that is, up to ~ 20 ppb Pt, 15 ppb Pd, 1 ppb Ir, 3 ppb Ru, 2 ppb Rh, and 3 ppb Au. Pd and Au show weakly developed negative correlations with MgO (Fig. 8a and b), consistent with an incompatible behavior of the two noble metals. In contrast to Pd and Au, the other PGE [Pt, Rh and the iridium-group PGE (IPGE)] show positive correlations with MgO (Fig. 8c–f), indicating compatible behavior. Compatible behavior of the IPGE is not uncommon in mafic–ultramafic rocks (Barnes *et al.*, 1985), but compatible behavior of Pt is rare (Park *et al.*, 2013).

The drill-core data show that the highest Pt values in unaltered rocks are around 150 ppb (Fig. 9). These values occur in a specific layer that can be correlated laterally for several hundred metres. Soil geochemistry (Prendergast, 2009) suggests that beyond that, the layer either pinches out or is buried. Some strongly elevated Pt values are also observed within the 2–20 m thick lateritic cover, in which Cu and Cr also show anomalously high values. It is notable that the highest Pt stream anomalies, in the centre of the KG1 intrusive body, do not correlate with elevated Pt in the soils. Possibly, the streams locally record residual Pt enrichment related to advanced weathering in a pronounced topographic gradient.

Of particular note are the high Pt/Pd ratios in the MdC (Pt/Pd mostly > 5), and the lack of correlation between Pt and Pd (Fig. 11b). This is in marked variance to what is observed in most other layered intrusions and mafic–ultramafic systems in general (Fiorentini *et al.*, 2012; Maier *et al.*, 2013). In contrast, Pt shows well-defined positive correlations with the IPGE and Rh (Fig. 11a, c and d). Different blocks and sub-blocks of the MdC define distinct correlations, with KG1 having a relatively Rh- and Pt-enriched population, whereas KG1 extension, KG3 and KG4 each define distinct populations.

Highly anomalous Pd values have been found in a single example of a sulfide-bearing quartz vein associated with an amphibolite xenolith in drill core MPD 001 (Supplementary Data Electronic Appendix 14). The sample contains up to 13.92 ppm Pd, 0.98% Cu, minor Au, 32 ppb Pt, and < 10 ppb Rh and Ru.

The mantle-normalized chalcophile element patterns for the orthopyroxenites and norites from all intrusive blocks (Supplementary Data Electronic Appendix 15) show a progressive increase from Ir to Pt, followed by a decreasing trend through Pd and Au to Cu. The ophitic gabbros show very different patterns, with a progressive increase from Ir to Cu, and a small negative Au anomaly. The amphibolites have bowl-shaped patterns with strong PGE depletion relative to Cu and Ni.

Plots of Cu/Pd and Cu/Zr versus MgO (wt %) (Fig. 12) allow an estimate of the fertility of the magmas. The Cu/Pd ratio of the orthopyroxenites and olivine pyroxenites is mostly around or below the level of the primitive mantle (PM), with outliers possibly explained by Pd mobility or localized and temporary sulfide saturation. The Cu/Pd ratios of the norites and gabbros tend to be slightly above PM values ($\sim 11\,000$), reflecting moderate Pd depletion of the magma. The amphibolites have Cu/Pd significantly above PM values and thus crystallized from a PGE-depleted magma that equilibrated with sulfide prior to solidification. The Cu/Zr ratio of most samples is 0.5–2, overlapping with that of South African continental flood basalts (Maier *et al.*, 2003), consistent with crystallization of the MdC rocks from a S-undersaturated parent magma. Some samples have higher Cu/Zr. They could contain small amounts of cumulus sulfide, consistent with their low Cu/Pd ratios. The PGE-depleted amphibolites have undepleted Cu/Zr values, suggesting that any sulfide that they equilibrated with was of low volume.

Sr and Nd isotopes

Strontium isotope data for plagioclase from two orthopyroxenites, one olivine pyroxenite and one gabbro-norite from KG1 and KG3 show remarkable homogeneity between samples as well as between intrusive blocks (Supplementary Data Electronic Appendices 3 and 16). The samples have $^{87}\text{Sr}/^{86}\text{Sr}_i$ 0.70255–0.70261 and positive ϵSr_T around +20.

The four samples analysed for whole-rock Nd isotope ratios (Supplementary Data Electronic Appendix 4)

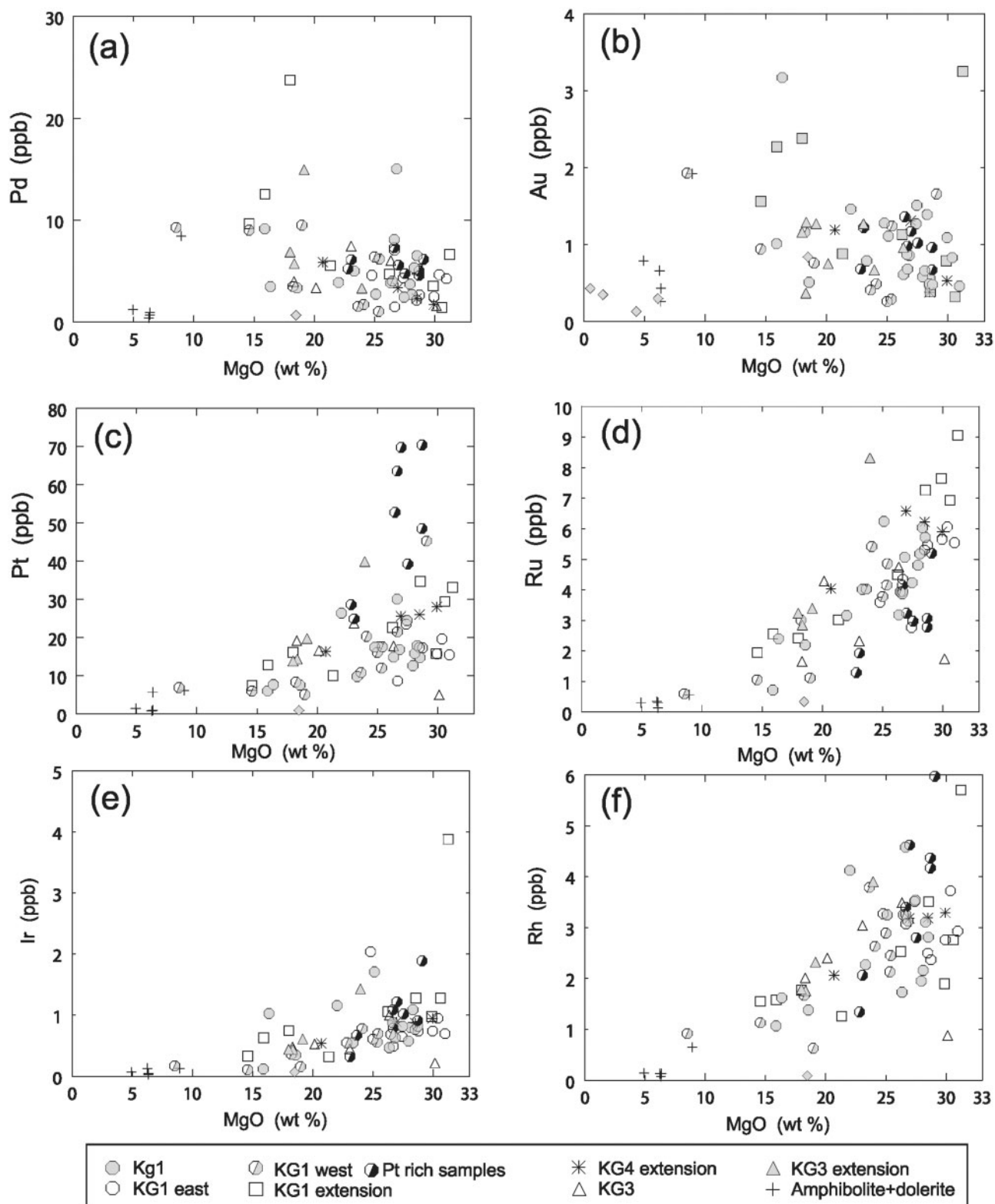


Fig. 8. Variation of chalcophile metals in various blocks of the Monts de Cristal Complex vs MgO: (a) Pd, (b) Au, (c) Pt, (d) Ru, (e) Ir, (f) Rh. (See text for discussion.)

have ϵNd_T -0.6 to 0.3 , showing little variation between samples and between intrusive blocks. The ophitic gabbro (DY18) has ϵNd of $+1.8$, suggesting magma derivation from a depleted mantle source.

X-RAY FLUORESCENCE MICROSCOPY

X-ray fluorescence microscopy has provided added insight into the crystallization history of the MdC rocks, allowing the location and identification of trace Pt-rich

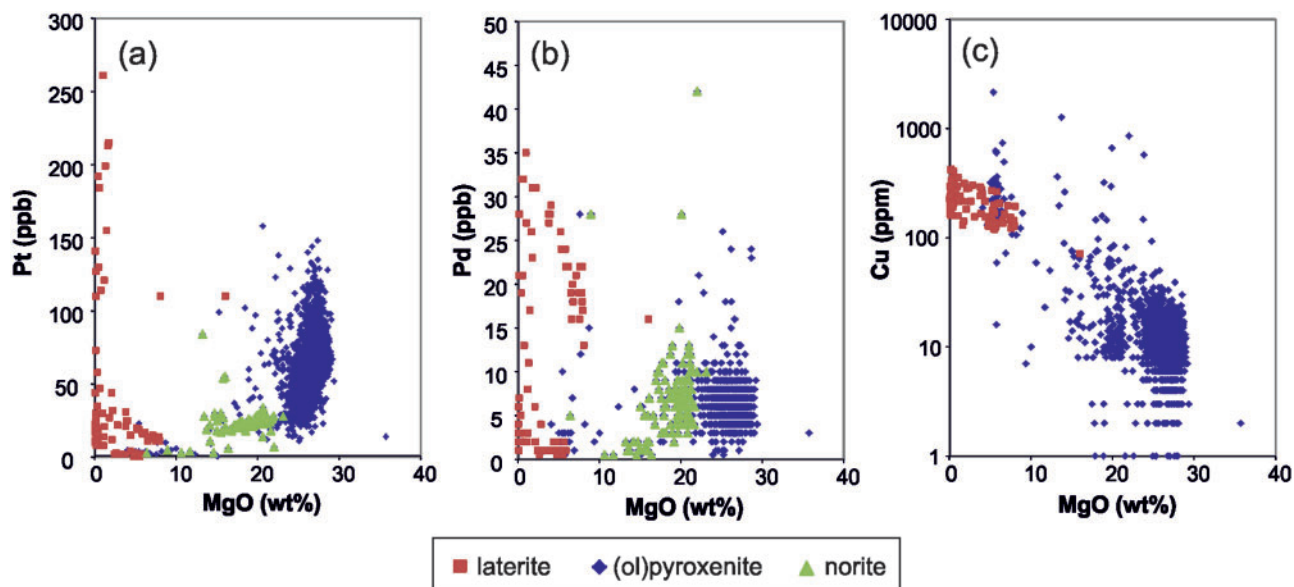


Fig. 9. Variation of (a) Pt, (b) Pd, and (c) Cu vs MgO (wt %) in drill-core samples.

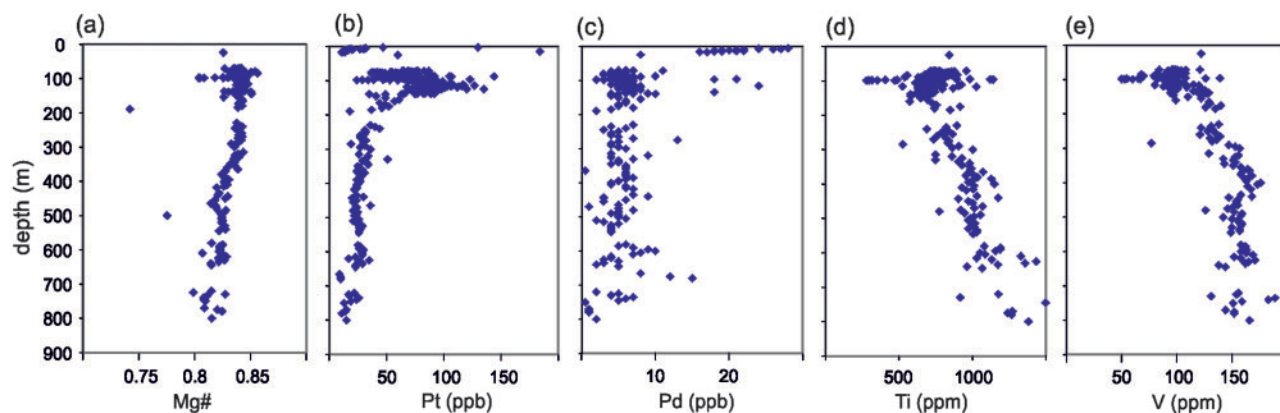


Fig. 10. Variation of Mg# (a), Pt (b), Pd (c), Ti (d) and V (e) in drill core MPD-005 as a function of depth.

phases. Figures 13 and 14 show two orthopyroxenite heteradcumulates containing cumulus orthopyroxene, ~5% plagioclase oikocrysts, minor intercumulus clinopyroxene and trace chromite and olivine inclusions within orthopyroxene.

More than a hundred small Pt-rich phases have been found in the five samples mapped, with at least 12 in each sample, suggesting that such phases are fairly common. The elevated Pt content across significant core intervals (e.g. 200 m with 50–100 ppb Pt in drill core MPD 001; Supplementary Data Electronic Appendix 13) suggests a relatively homogeneous distribution of these phases, which in turn suggests that there are few large grains. Such grains would be systematically under-sampled during petrographic analysis (Godel, 2013) and are unlikely to be detected by conventional methods.

The Pt phases located in the two samples reported in detail in this study are all less than 10 μm in size. The precise location in relation to the host grain boundary is

difficult to determine precisely, owing to the unknown shape of the grain boundary in the third dimension, but it appears that all the Pt phases occur at or within a few tens of microns of the margins of orthopyroxene grains. Although the sample size is currently too small to be sure, none of the Pt phases was located within the Cr-zoned, chromite-bearing pyroxene grains, and their occurrence is apparently regardless of whether the host grain has a Ti-enriched rim. The great majority of grains so far identified fall at or close to the margins of orthopyroxene grains enclosed within plagioclase oikocrysts. This implies that the Pt phase or phases crystallized at the cumulus stage, but there is no association with chromite inclusions, as might have been predicted from the model of Finnigan *et al.* (2008).

The nature of the Pt-rich phases remains uncertain; all of the grains located so far lie beneath the surface of the host sample, and none have yet been observed optically or by SEM. Identification is therefore based on the element association obtained from the XFM data.

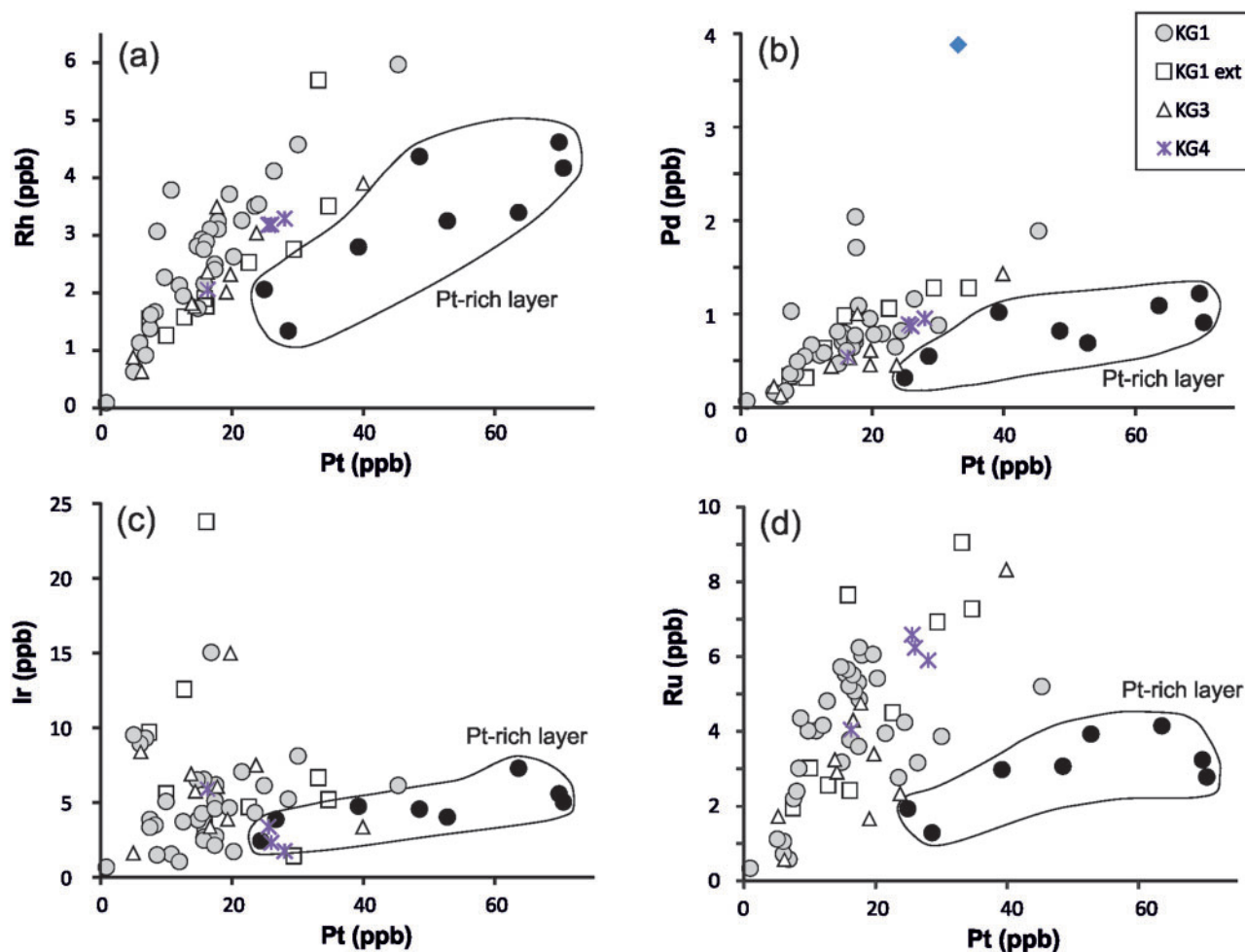


Fig. 11. Variation of Rh (a), Pd (b), Ir (c) and Ru (d) vs Pt for the MdC Complex. Outlined fields mark samples from a Pt-rich layer at KG1 west.

About 50% of Pt grains show an association with As. For example, in sample Px21a there are two clusters of Pt grains, one associated with As, the other associated (but not co-located) with Ni and Cu. Approximate estimation of the depth of the grain in the sample in each case, based on variability of the apparent Pt peak height across the Maia detector array (Barnes *et al.*, in preparation), indicates that in most cases Pt and As are co-located whereas the Ni–Cu peaks, attributed to sulfide phases, are slightly offset from Pt and As in three dimensions. The semi-quantified data indicate that in some, but not all, cases the visible coincident As and Pt spots on the map correspond approximately to sperrylite stoichiometry, PtAs₂. It is likely that at least some of the Pt grains are sperrylite. However, Pd is not detected by this technique, and neither is Te, although Bi is detectable and none of the observed grains show any Bi association. Further investigation is continuing to increase the sample size of detected grains, and to locate these phases.

The small sulphide grains associated in some cases with the Pt-rich phases could have formed in response to reaction of the platinum group metals (PGM) with

S-saturated trapped liquid, or S-bearing hydrous fluid, although there is no evidence for magmatic hydrous phases within these samples. The great majority of the 100+ grains so far identified are therefore attributable to direct magmatic precipitation of sperrylite and/or other Pt-dominant phases, thought most likely to be Pt–Fe alloys.

GEOCHRONOLOGY

Twelve analyses were made of six baddeleyite grains (Supplementary Data Electronic Appendices 17 and 18). The data are scattered in ²⁰⁶Pb/U and most are apparently discordant, which is presumed to be due to grain orientation effects. They are closely grouped in ²⁰⁷Pb/²⁰⁶Pb, giving a weighted mean age of 2775 ± 11 Ma. However, there is some excess scatter (MSWD = 2.6). Low-side culling makes little difference to the MSWD and high-side culling reduces it to <0.7, implying overculling. Given the modest size of the dataset, the variable precision of the ²⁰⁷Pb/²⁰⁶Pb data and the lack of a clear justification for any data rejection, we adopt the most conservative option, retaining all data

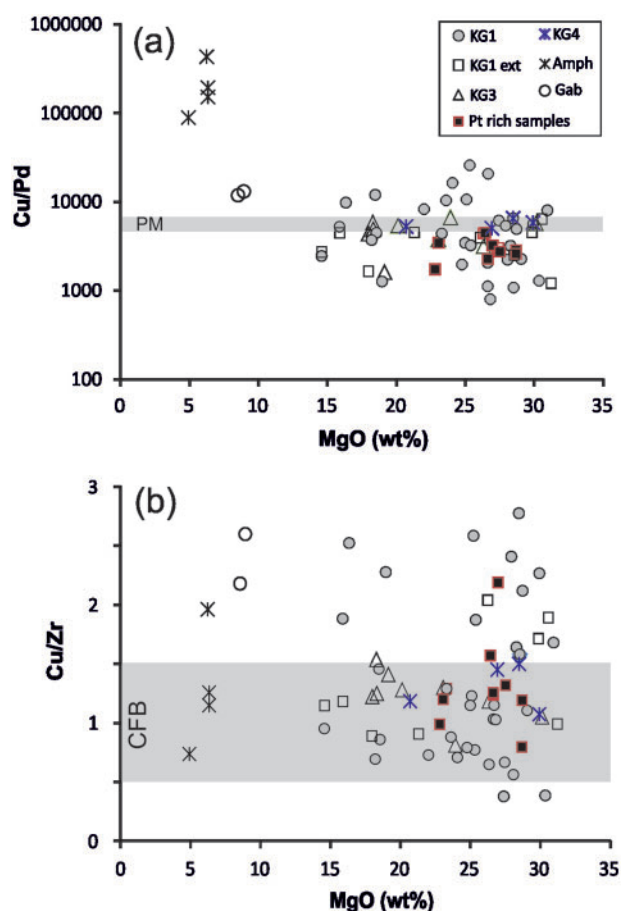


Fig. 12. Cu/Pd and Cu/Zr vs MgO (wt %) for the Monts de Cristal rocks. Primitive mantle (PM) estimate in (a) is from Barnes & Maier (1999). Shaded bar in (b) represents the range of South African continental flood basalts [CFB, from Maier *et al.* (2003)].

and hence taking the age of baddeleyite crystallization to be 2775 ± 11 Ma.

Ten analyses were obtained from four monazite grains (Supplementary Data Electronic Appendices 19 and 20). The majority of the results are apparently 5–6% discordant; however, the consistency of the offset from concordia implies that this is due to a bias in Pb/U, possibly owing to an unidentified matrix effect. The variability of minor element contents and lack of Y data make this impossible to assess, particularly for the one strongly discordant point, which is from a very high Th sample.

The data appear to fall into three categories. There are three points that are close to concordia and may be from concordant samples that have essentially identical $^{207}\text{Pb}/^{206}\text{Pb}$. One other analysis matches this $^{207}\text{Pb}/^{206}\text{Pb}$ but is >10% discordant. This analysis had low CePO_2^+ counts and a very high Th content, suggesting that the spot inadvertently incorporated some huttonite. If this is true, the different (mixed) matrix might explain the apparent discordance. It is also possible that huttonite is metamict and has undergone ‘recent’ Pb loss, and therefore that the analysed volume is genuinely

discordant. These four analyses come from four distinct sample grains. The weighted mean $^{207}\text{Pb}/^{206}\text{Pb}$ dates for all four analyses is 2767 ± 7 Ma (including uncertainty propagated from the $^{207}\text{Pb}/^{206}\text{Pb}$ reference sample PD-95 that was used for mass fractionation correction), or 2766 ± 9 Ma if only the three most concordant analyses are used. A fifth analysis is $\sim 2\sigma$ from the main cluster; incorporating it into the weighted mean gives 2765 ± 11 Ma, with only minor excess scatter (MSWD = 1.5).

The other data scatter along a trend that might be a mixing discordia. The trend is too short and Pb/U too susceptible to matrix-induced errors for a lower intercept to be defined. However, it is almost inescapable to conclude that there has been at least one younger episode of monazite growth or recrystallization. Therefore the monazite gives a minimum age of 2765 ± 11 Ma for the orthopyroxenite, consistent with the baddeleyite date.

DISCUSSION

Parent magma composition

The composition of the MdC parent magma remains difficult to constrain. We used two semi-quantitative approaches. First, we searched the literature to identify other examples of orthopyroxenite cumulates of broadly similar composition to those of the MdC Complex, particularly those for which parent magma estimates are available. A relatively good compositional overlap exists with Bushveld orthopyroxenites (Fig. 6, and Supplementary Data Electronic Appendix 11). We simulated the crystallization of the Bushveld B1 magma using PELE software (Boudreau, 1999). A particularly good fit with the MdC rocks is provided by sample ECBV106 (Barnes *et al.*, 2010; 10.07% MgO) at quartz-fayalite–magnetite (QFM) and 100 bar. The simulation yields spinel as the first mineral to crystallize, followed by olivine (Fo85), orthopyroxene (En86, after 10% crystallization) and then plagioclase (An69). Second, for one of our best characterized and least evolved samples (Px21) we determined modal proportions by point counting, and then subtracted the amount of MgO hosted by orthopyroxene from the whole-rock composition. This method gave 8% MgO for the intercumulus component; however, it needs to be borne in mind that this value is potentially affected by residual liquid percolation.

To obtain a rough idea about the concentration of incompatible minor and trace elements in the trapped melt we have plotted best-fit lines through variation diagrams versus MgO for the ultramafic rocks (Supplementary Data Electronic Appendix 21) and recorded the trace element concentration at 10% MgO (TiO_2 0.4–0.5%, La ~ 8 ppm, Ce ~ 10 ppm, Sm ~ 1 –1.5 ppm, Th 2 ppm, Zr 40–60 ppm, Ta 0.15 ppm, and Y 10–12 ppm). These data suggest that the MdC magma was a magnesian basalt with $\sim 10\%$ MgO, a relatively low TiO_2 content of around 0.5 wt % and relatively high

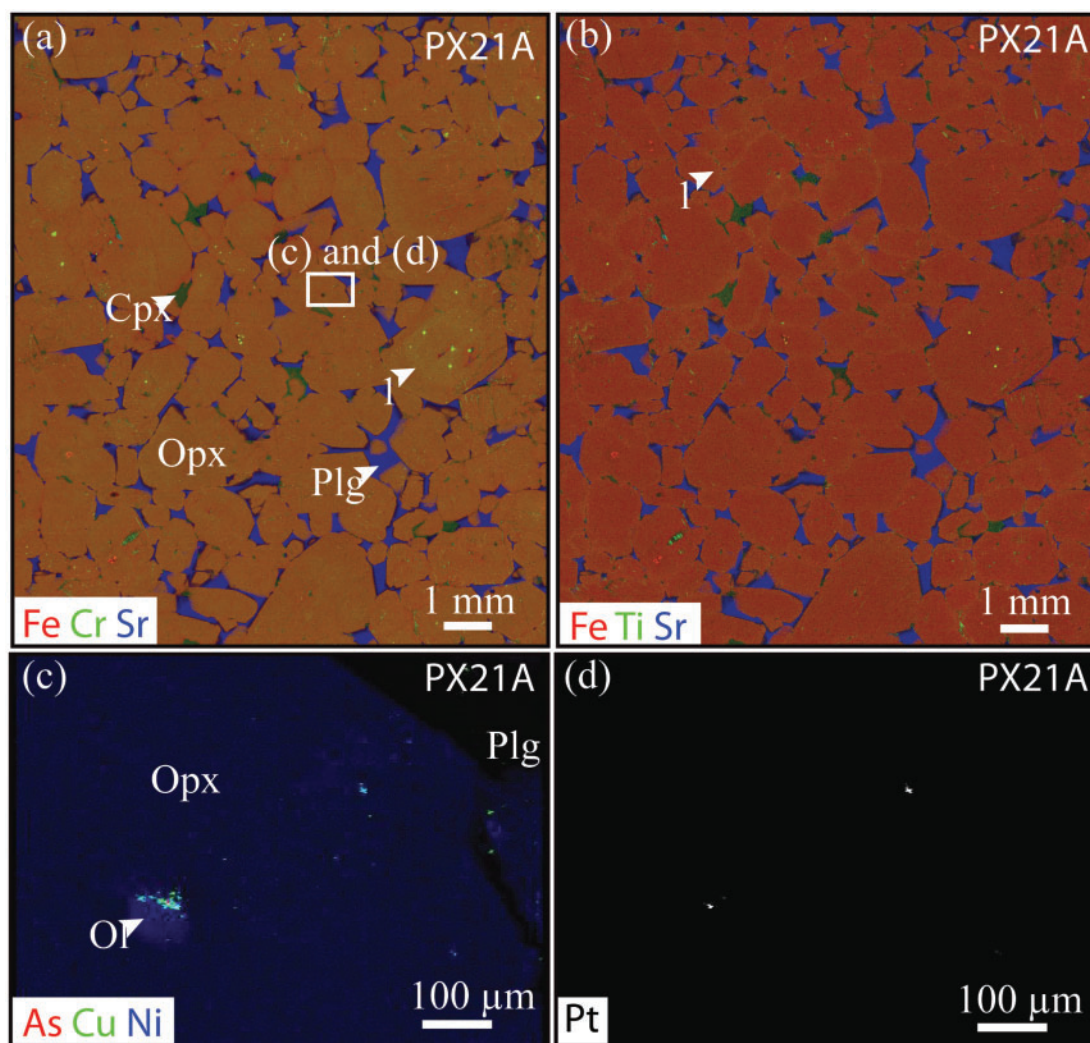


Fig. 13. (a, b) Three-element false-colour RGB images of sample Px21 a. Each element is scaled to maximum values; Cr and Ti values are log transformed to enhance the compositional range within the silicate phases. The heteradcumulate texture of plagioclase oikocrysts (blue on both images) interstitial to orthopyroxene and minor intercumulus clinopyroxene (green on both images) should be noted. Other noteworthy features are the subtle complex internal zoning in Cr in some grains [grain 1 in (a)] and fine rims of elevated Ti in (b) in areas outside the plagioclase oikocrysts [point 1 in (b)]. Light green highlights on both images are small chromite inclusions, preferentially located in grains showing Cr zoning. (c) Three-element image for As (red)–Cu (green)–Ni (blue); light green areas indicate the probable presence of Cu–Ni-rich sulphide. One of these sulfide areas occupies the grain boundary between the opx host and an olivine inclusion. The presence of isolated small Cu-rich phases, probably sulphide, with no associated Pt or As, at the opx margin should be noted. (d) Pt peaks correspond to coincident highs for As, within areas enriched in Cu and Ni, but not exactly matching Cu–Ni peaks. Pt corresponds exactly to the As peak in each case.

concentrations of other incompatible trace elements. TiO_2/La ratios are comparable with those of continental flood-type basalts with similar MgO contents (e.g. Ventersdorp and Dominion; Marsh *et al.*, 1989, 1992). The whole-rock trace element data can be modeled by up to 20% combined assimilation–fractionation crystallization (AFC) of parental basalt (with trace element contents assumed to be $4 \times$ primitive mantle; i.e. equivalent to $\sim 25\%$ partial mantle melting) with a 17% partial melt of MdC country rock granite (average of samples GRA 2W and GRA 2X; Supplementary Data Electronic Appendix 2). The composition of the granitic partial melt was calculated by assuming restite modal proportions determined in melting experiments of biotite gneiss at 875°C and 3 kbar (Patiño Douce & Beard,

1995), and D values summarized by Rollinson (2013) (Fig. 15). However, as the model contains a large number of variables, other interpretations are possible, including a magma source in metasomatized mantle.

The Nd and Sr isotope data are broadly consistent with the interpretations from the trace element data. Assuming that the host granites had Sr_i of 0.7013 at 3120 ± 67 Ma (Rb/Sr whole-rock method; Caen-Vachette *et al.*, 1988), and $\epsilon_{\text{Nd}} 0.2$ (i.e. approximately CHUR_T), and that the MdC magma was a magnesian basalt with $4 \times$ PM levels of Rb, Sr, Sm and Nd (Sun & McDonough, 1989), Sr_i 0.701 , and $\epsilon_{\text{Nd}} 2.1$ (depleted mantle, DM; DePaolo, 1981), the MdC samples (Sr_i 0.70255 – 0.70261 , ϵ_{Nd} 0.3 to -0.6) can be modeled by 10–15% bulk contamination with the host granite. Unfortunately,

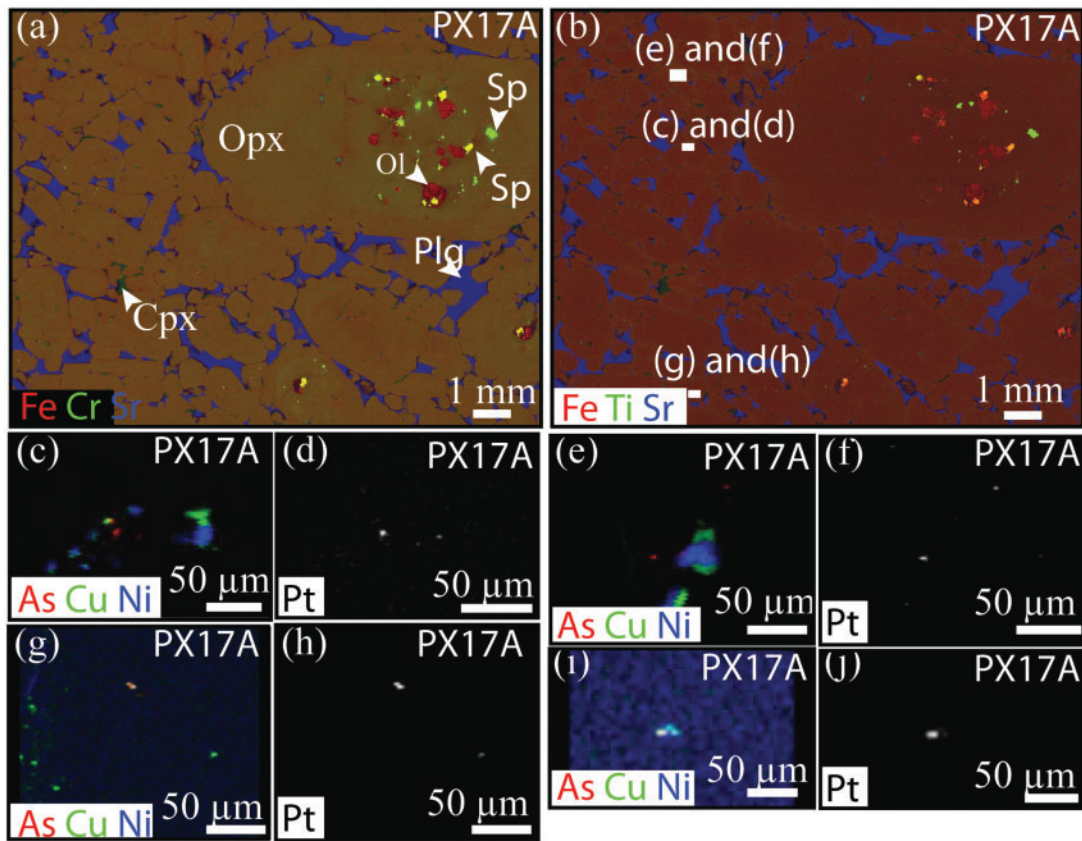


Fig. 14. Sample Px17A, with the same combinations of elements as in Fig. 13a. The abundant inclusions of olivine (red) and chromite (green) in Cr-zoned opx should be noted. No Pt grains were found in this grain, however. Enlarged areas show As–Cu–Ni three-element maps as above, and corresponding single-element concentration maps for Pt. It should be noted that in all areas Pt hits are associated with areas containing all three elements (As, Cu and Ni), but the Pt peaks are very specifically associated with As, and do not necessarily occur directly within what appear to be sulphide aggregates. These aggregates are all occurring at or indistinguishably close to opx grain boundaries, but with no systematic relationship to plagioclase oikocrysts.

Caen-Vachette *et al.* (1988) did not provide detailed information on sampling sites or trace element geochemistry, and their Rb–Sr dates have large uncertainties, which renders the above modeling semi-quantitative at best. To improve the reliability of the model, high-precision geochronology, isotope geochemistry and trace element data of the host granites would be required.

The two ophitic gabbro samples cannot represent the parent magma to the orthopyroxenites and norites, as the gabbros have distinctly less fractionated trace element patterns and less enriched Nd isotope signatures, as well as depleted PGE contents ($\text{Cu/Pd} > 7000$). Whether the gabbros do indeed belong to the same magmatic event as the remainder of the MdC cumulates needs to be confirmed by dating.

Nature of PGE enrichment and PGE host phases

The Pd levels of most of the MdC ultramafic samples can be modeled by assuming that the rocks contain 10–30% trapped liquid (broadly consistent with petrography) with 20–25 ppb Pd. Such levels are at the upper end globally of Pd contents in basalts (Fiorentini *et al.*, 2010; Maier *et al.*, 2013). Other examples of Pd-rich basalts include Finnish 2.45 Ga tholeiitic dykes with up to

30–35 ppb (Guo *et al.*, 2012), and Svecofennian basalts with up to 25 ppb (Barnes *et al.*, 2009).

In contrast to Pd, the measured Pt contents of the MdC cumulates are far too high to be explained by a trapped liquid component. Our global database indicates that basaltic magmas may contain up to ~20 ppb Pt (Maier *et al.*, 2013). A 30% trapped liquid component could thus account for no more than 6–7 ppb Pt. Hydrothermal introduction of Pt or removal of Pd and S after crystallization is considered unlikely, in view of the relatively homogeneous nature of the PGE contents in the MdC along its ~100 km strike, and the generally unaltered nature of the rocks. Localized mobility of Pd is indicated by the development of vein-style mineralization, but this is extremely rare and closely associated with amphibolite xenoliths.

A more likely scenario is that the MdC magma had Pt contents in the range of other basalts (15–20 ppb), but reached Pt (or PtAs_2) saturation prior to sulfide saturation. This model is consistent with the synchrotron XFM data reported above and the low S contents of the MdC rocks (Fig. 7). Compatible behavior of Pt has previously been reported from other basaltic suites, including the Pual Ridge (Park *et al.*, 2013), where it was assigned to precipitation of Pt alloys.

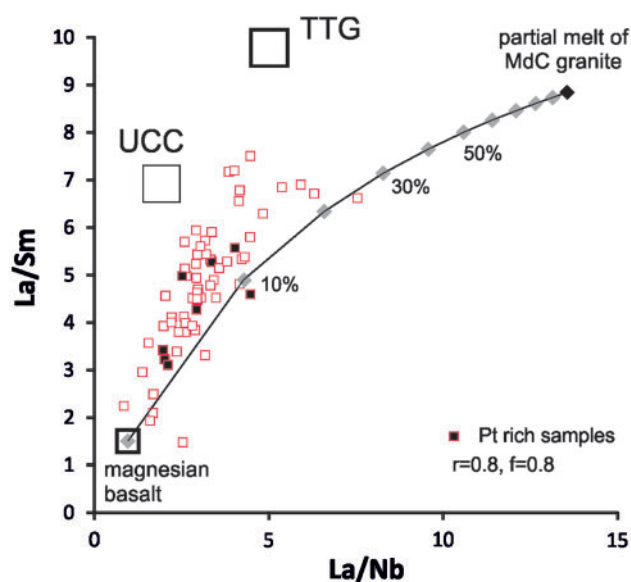


Fig. 15. Variation of La/Sm vs La/Nb for the MdC rocks. Also plotted is average upper continental crust (UCC; Rudnick & Fountain, 1995) and average 3.0–3.5 Ga tonalite–trondhjemite–granodiorite (TTG; Martin *et al.*, 2005). Continuous line represents a mixing line between a magnesian basalt and a contaminated magma produced by AFC ($r=0.8$, $f=0.8$) of magnesian basalt with a 17% partial melt of MdC country rock granite. Trace element contents of magnesian basalt are assumed to be $4 \times$ that of primitive mantle (PM), with PM data taken from McDonough & Sun (1995). (See text for further discussion.)

As platinum shows well-defined positive correlations with Ir, and to a lesser extent Ru and Rh (Fig. 11), these metals also appear to have been compatible during fractionation. Compatibility of IPGE in mafic–ultramafic rocks has been described in many igneous suites (Barnes *et al.*, 1985; Puchtel & Humayun, 2001). From a crystal-chemical point of view, the IPGE could be hosted by orthopyroxene and olivine, substituting for Mg in octahedral coordination; this has been shown to be the case for Ru, Rh and Ir in olivine (Brenan *et al.*, 2003, 2005). Several studies have proposed that in mafic–ultramafic rocks the IPGE are mainly hosted by Os–Ir–Ru alloys and PGM (e.g. Peck & Keays, 1992), but as yet no IPGE-enriched PGM have been identified in the MdC. Another possible host for the IPGE is chromite (Locmelis *et al.*, 2011; Pagé *et al.*, 2012), but chromite is rare in the MdC and thus unlikely to control IPGE distributions, at least in the form of solid solution. Some of the IPGE and Rh could be hosted in Pt alloys. For example, Pt alloys described by Garuti *et al.* (2002) have approximately 80% Pt, and 1–2% Ir, Ru, and Rh. However, in the MdC we do not see any detectable IPGE associated with the As phases.

Factors controlling Pt saturation

PGE levels in basaltic magmas depend largely on the solubility of sulfide liquid, platinum-group minerals and PGE alloys during mantle melting and fractional crystallization in the crust. Small- to medium-degree

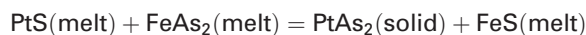
(<10–20%) melts of asthenospheric mantle are saturated in sulfide (Barnes *et al.*, 1985; Rehkämper *et al.*, 1999; Mungall & Brenan, 2014) and thus depleted in all PGE. Upon dissolution of mantle sulfides at larger degrees of melting, the concentrations of each of the PGE in the magma depend on whether sulfide is the main PGE host phase or whether, in addition, any PGM or PGE alloy is stable. Palladium is controlled only by sulfide and thus large-degree mantle melts such as komatiites have Pd levels 2–3 times that of the primitive mantle (Fiorentini *et al.*, 2013). Platinum levels additionally depend on whether Pt alloy is stable, which in turn is controlled by T , fO_2 and depth of melting (Mungall & Brenan, 2014). At relatively low pressure, Pt alloy is stable even for high-degree melting, resulting in subchondritic Pt/Pd ratios in most asthenospheric mantle-derived magmas [e.g. mid-ocean ridge basalt (MORB) and komatiites]. Increased temperature, fO_2 and melting depth enhance Pt alloy solubility (Borisov & Palme, 1997; Fortenfant *et al.*, 2003; Mungall & Brenan, 2014), leading to a decrease in the bulk partition coefficient of Pt. This should result in relatively high Pt/Pd in the melt, perhaps approaching the chondritic ratio as observed in Bushveld magmas. However, it is notable that globally mantle melts mostly have Pt contents between 10 and 15 ppb (Maier *et al.*, 2009; Fiorentini *et al.*, 2010), with very few examples of higher values that might be expected in high-degree melts generated at high pressure. This is probably due to the fact that the Pt contents of the magmas are capped by decreasing Pt solubility during magma ascent, resulting in the precipitation of Pt alloys or PGM.

Enigmatically, the empirical data indicate much higher Pt solubilities in mafic magmas (10–15 ppb) than the available experimental data. Thus, Ertel *et al.* (1999) showed that Pt solubility in basalt is as low as 3 ppb. Borisov & Palme (1997) proposed higher values, around 15 ppb, but their experiments probably overestimate the Pt solubility as they involved bulk analyses in which samples may have been contaminated with undissolved Pt particles. The mismatch between the natural magmas and the experimental data suggests that either the solubility model is wrong or other factors play a role. The experiments of Borisov & Palme (1997) and Ertel *et al.* (1999) were conducted on synthetic basalts that contained no Fe or S; Fe addition should result in the formation of Pt alloys and thus relatively lower Pt solubility (Borisov & Palme, 2000). However, Laurenz *et al.* (2013) have shown that the presence of sulfur in magmas significantly increases Pd and Ru solubility, and Mungall & Brenan (2014) have suggested a similar effect on Pt.

Of particular interest is the origin of the Pt-enriched layer of the MdC (Fig. 10, and Supplementary Data Electronic Appendix 13). The Pt-rich samples are heteroaccumulates that largely lack chromite and olivine. They have the highest Mg# (i.e. are the least evolved) but in terms of petrography, isotope composition and incompatible trace element ratios they are

compositionally indistinguishable from the other rocks. Owing to the small size of the Pt phases identified, gravitational concentration from convecting magma seems unlikely, unless the Pt phases nucleated on the surface of cumulus orthopyroxene grains and were mechanically concentrated with them. The Pt solubility could have been temporarily lowered owing to reduction of the magma in response to wall-rock contamination; however, not only would this potentially have triggered sulfide saturation (Tomkins *et al.*, 2012), but also it is inconsistent with the V contents of the rocks. The experimental data of Toplis & Corgne (2002) have shown that partitioning of V into pyroxene increases with falling oxygen fugacity. Thus, one would expect an increase in V to accompany the Pt enrichment, contrary to the observations from the drill-core data that show inflections towards low V contents in the Pt rich layer. Furthermore, there is no lithological evidence such as the presence of country rock xenoliths that could suggest local magma contamination in the Pt-enriched horizon. Localized reduction owing to chromite crystallization (Finnigan *et al.*, 2008) can be ruled out because the most Pt-rich samples are chromite poor, and no Pt phases were observed by XFM mapping in contact with chromite grains. The available evidence suggests that the formation of the Pt-enriched layer is related to magma replenishment with relatively unevolved magma, consistent with a subtle increase in Mg# and a decrease in V and Ti of the rocks.

An additional factor suggested by our observations is that arsenic plays a role in the stability of magmatic Pt phases. The evidence for primary precipitation of Pt–As-rich phases, thought to be sperrylite, suggests that the key factor may be the magma exceeding the solubility product for sperrylite. If Pt is dissolved in the magma as PtS, as implied by the experimental data of Mungall & Brenan (2014), then the following reaction may be operating:



with the reaction being driven by the increasing activity coefficient of PtS with falling temperature along a given $f\text{O}_2$ buffer implied by the Mungall & Brenan experiments. This conjecture requires testing by investigation of the solution properties of Pt in the presence of As in silicate melts, which are currently unknown. The divergence of the Pt/Pd ratio noted in a number of layered intrusions and mafic lava suites (e.g. Stillwater, Keays *et al.*, 2012; Deccan Trap lavas, Keays & Lightfoot, 2010) may be explained by preferential fractionation of magmatic Pt arsenides.

Unfortunately, no arsenic data are available to evaluate whether the elevated Pt contents in the MdC rocks could be due to unusually high As concentrations in the magma. However, assuming that all of the Pt occurs as PtAs₂, with overall Pt levels at ~20–150 ppb, this would require ~15–100 ppb As for charge balance. This is in the range of As contents reported by Jenner & O'Neill (2012) for MORB in the 8–10 wt % MgO range (~125 ppb

As). Hence, the required As contents implied by the Pt contents of the rocks are not exceptional, adding support to the notion that Pt-arsenide might be more significant in S-poor rocks than previously supposed (J. Brenan, personal communication, 2015).

CONCLUSIONS

The Monts de Cristal Complex of Gabon is a large layered intrusion, approximately 100 km long and 1–3 km wide. It consists predominantly of orthopyroxenite that crystallized from a low-Ti basalt with ~10% MgO. The complex is characterized by strong enrichment in Pt (up to 150 ppb) relative to Pd (<20 ppb) and other chalcophile elements and sulphur. X-ray fluorescence microscopy has identified numerous small (<10 μm) Pt-rich phases, mostly arsenides. This is interpreted to indicate precipitation of Pt-arsenides from an S-undersaturated magma, constituting some of the best evidence yet for direct crystallization of platinum-group minerals from basaltic magmas.

ACKNOWLEDGEMENTS

We thank Sari Forss for producing thin sections, Leena Järvinen and Arto Pulkkinen for assistance with Sm–Nd isotope analysis, and Chris Ryan, Martin de Jonge and Daryl Howard for assistance and support in the XFM mapping component of this research, which was undertaken on the XFM beamline at the Australian Synchrotron, Victoria, Australia. C. Li and J.-W. Park engaged in helpful discussions on S and Pt saturation. Lonmin is thanked for granting permission to publish the findings of our research and the geochemical data on the drill cores. Martin Prendergast allowed the use of his field map in Fig. 2. Discussions with Sarah-Jane Barnes and constructive reviews by Chusi Li and James Brenan helped to improve the paper significantly.

FUNDING

The work undertaken on the X-ray fluorescence microscopy beam line at the Australian Synchrotron, Clayton, Victoria, Australia, was supported by grant AS6618 to B.G. SJB, and WDM. We further acknowledge financial support to Barnes and Godel from the CSIRO Office of the Chief Executive, and financial support for the Australian Synchrotron facility from the Science and Industry Endowment Fund (SIEF).

SUPPLEMENTARY DATA

Supplementary data for this paper are available at *Journal of Petrology* online.

REFERENCES

- Arsandaux, H. (1912). Sur la presence au Gabon de roches appartenant à la série de la charnockite. *Comptes Rendus de l'Académie des Sciences* **154**, 896–898.
- Aubague, M. & Hausknecht, J. J. (1959). *Carte géologique de reconnaissance au 1/500 000, feuille Libreville Est. Carte et notice explicative*. Direction des Mines et de la Géologie de l'AEF, 34 pp.
- Barnes, S.-J. & Maier, W. D. (1999). The fractionation of Ni, Cu and the noble metals in silicate and sulphide liquids. In: Keays, R. R., Leshner, C. M., Lightfoot, P. C. & Farrow, C. E. G. (eds) *Dynamic Processes in Magmatic Ore Deposits and their Application to Mineral Exploration*. Geological Association of Canada, *Short Course Notes* **13**, 69–106.
- Barnes, S. J. & Naldrett, A. J. (1986). Geochemistry of the J-M Reef of the Stillwater Complex, Minneapolis Adit area II. Silicate mineral chemistry and petrogenesis. *Journal of Petrology* **27**, 791–825.
- Barnes, S.-J., Naldrett, A. J. & Gorton, M. P. (1985). The origin of the fractionation of platinum-group elements in terrestrial magmas. *Chemical Geology* **53**, 303–323.
- Barnes, S. J., Makkonen, H. V., Dowling, S. E., Hill, R. E. T. & Peltonen, P. (2009). The 1.88 Ga Kotalahti and Vammala nickel belts, Finland: geochemistry of the mafic and ultramafic metavolcanic rocks. *Bulletin of the Geological Society of Finland* **81**, 103–141.
- Barnes, S.-J., Maier, W. D. & Curl, E. A. (2010). Composition of the marginal rocks and sills of the Rustenburg layered suite, Bushveld Complex, South Africa: Implications for the formation of platinum-group element deposits. *Economic Geology* **105**, 1491–1511.
- Barnes, S. J., Osborne, G. A., Cook, D., Barnes, L., Maier, W. D. & Godel, B. (2011). The Santa Rita nickel sulfide deposit in the Fazenda Mirabela Intrusion, Bahia, Brazil: Geology, sulfide geochemistry and genesis. *Economic Geology* **106**, 1083–1110.
- Barnes, S. J., Van Kranendonk, M. J. & Sonntag, I. (2012). Geochemistry and tectonic setting of basalts from the Eastern Goldfields Superterrane. *Australian Journal of Earth Sciences* **59**, 707–735.
- Borisov, A. & Palme, H. (1997). Experimental determination of the solubility of platinum in silicate melts. *Geochimica et Cosmochimica Acta* **20**, 4349–4357.
- Borisov, A. & Palme, H. (2000). Solubilities of noble metals in Fe-containing silicate melts as derived from experiments in Fe-free system. *American Mineralogist* **85**(11–12), 1665–1673.
- Boudreau, A. E. (1999). PELE—a version of the MELTS software programme for the PC platform. *Computers and Geosciences* **25**, 201–203.
- Brenan, J. M., McDonough, W. F. & Dalpé, C. (2003). Experimental constraints on the partitioning of rhenium and some platinum-group elements between olivine and silicate melt. *Earth and Planetary Science Letters* **212**, 135–150.
- Brenan, J. M., McDonough, W. F. & Ash, R. (2005). An experimental study of the solubility and partitioning of iridium, osmium and gold between olivine and silicate melt. *Earth and Planetary Science Letters* **237**, 855–872.
- Caen-Vachette, M., Vialette, Y., Basset, J. P. & Vidal, P. (1988). Apport de la géochronologie isotopique à la connaissance de la géologie gabonaise. *Chronique de la Recherche Minière* **491**, 35–53.
- Campiglio, C., Marion, C. & Vannier, M. (1983). Le complexe mafique-ultramafique de M'Bilan. Etude des premiers échantillons de roches et de concentrés alluvionnaires. In: *Annexes, Rapport Cellule d'Orientation de l'Inventaire Minier, CGGM*. Direction des Mines et de la Géologie Minière du Gabon, 22 pp.
- Chevalier, L., Makanga, J. F. & Thomas, R. J. (2002). *Carte géologique de la République Gabonaise. Notice explicative*. Council for Geoscience, 195 pp.
- DePaolo, D. J. (1981). Neodymium isotopes in the Colorado Front Range and crust–mantle evolution in the Proterozoic. *Nature* **291**, 684–687.
- Edou-Minko, A., Grandin, G. & Campiglio, C. (2002). Pétrologie et géomorphologie dans la région de Kango, Gabon: un grand dyke ultramafique–mafique archéen. *Journal of African Earth Sciences* **32**, 899–918.
- Ertel, W., O'Neill, H. St, C. Sylvester, P. J. & Dingwell, D. B. (1999). Solubilities of Pt and Rh in a haplobasaltic melt at 1300°C. *Geochimica et Cosmochimica Acta* **63**, 2439–2449.
- Finnigan, C. S., Brenan, J. M., Mungall, J. E. & McDonough, W. F. (2008). Experiments and models bearing on the role of chromite as a collector of platinum group minerals by local reduction. *Journal of Petrology* **49**, 1647–1665.
- Florentini, M. L., Barnes, S. J., Leshner, C. M., Heggie, G. J., Keays, R. R. & Burnham, O. M. (2010). Platinum group element geochemistry of mineralized and nonmineralized komatiites and basalts. *Economic Geology* **105**, 795–823.
- Florentini, M. L., Barnes, S. J., Maier, W. D. & Heggie, G. J. (2012). Global variability in the PGE contents of komatiites. *Journal of Petrology* **52**, 82–112.
- Fletcher, I. R., McNaughton, N. J., Davis, W. J. & Rasmussen, B. (2010). Matrix effects and calibration limitations in ion probe U–Pb and Th–Pb dating of monazite. *Chemical Geology* **270**, 31–44.
- Fortenfant, S. S., Gunther, D., Dingwell, D. B. & Rubie, D. C. (2003). Temperature dependence of Pt and Rh solubilities in a haplobasaltic melt. *Geochimica et Cosmochimica Acta* **67**, 123–131.
- Garuti, G., Pushkarev, E. V. & Zaccarini, F. (2002). Composition and paragenesis of Pt alloys from chromitites of the Uralian–Alaskan-type Kytlym and Uktus complexes, northern and central Urals, Russia. *Canadian Mineralogist* **40**, 1127–1146.
- Godel, B. (2013). High-resolution X-ray computed tomography and its application to ore deposits: from data acquisition to quantitative three-dimensional measurements with case studies from Ni–Cu–PGE deposits. *Economic Geology* **108**, 2005–2019.
- Guo, F., Maier, W. D., Vuollo, J., Junttila, H. (2012). PGE-rich 2.45 Ga mafic dykes in northern Finland: implications for the origin of PGE mineralization in associated layered intrusions. Abstr., 12th Int Ni–Cu–PGE symposium, State Key Laboratory of Ore Deposit Geochemistry, Institute of Geochemistry, Chinese Academy of Sciences, Guiyang, China, p. 108–111.
- Huhma, H., Kontinen, A., Mikkola, P., Halkoaho, T., Hokkanen, T., Hölttä, P., Juopperi, H., Konnunaho, J., Luukkonen, E., Mutanen, T., Peltonen, P., Pietikäinen, K. & Pulkkinen, A. (2012). Sm–Nd results on the Archean crust in Finland. In: Hölttä, P. (ed.) *The Archean of the Karelia Province in Finland*. Geological Survey of Finland, *Special Paper* **54**, 176–213.
- Jenner, F. E., and O'Neill, H. S. C. (2012). Analysis of 60 elements in 616 ocean floor basaltic glasses, *Geochem. Geophys. Geosyst.*, **13**, Q02005, doi: 10.1029/2011GC004009.
- Kassa-Mombo, C., Minko-Bidza, V., Mikhailoff, N., Greenish, T., Devos, W., Boldrachi, R., Degroote, V., Bonnot, H., Adlof, L., Mabilia, R., Melchior, A. & Abeme, M. J. (1988). Apport de l'inventaire aux connaissances géologiques et minières des

- feuilles a 1/200 000 de Libreville, Kango et Lambarene (Gabon). *Chronique de la Recherche Minière* **491**, 105–124.
- Keays, R. R. & Lightfoot, P. C. (2010). Crustal sulfur is required to form magmatic Ni–Cu sulfide deposits; evidence from chalcophile element signatures of Siberian and Deccan Trap basalts. *Mineralium Deposita* **45**, 241–257.
- Keays, R. R., Lightfoot, P. C. & Hamlyn, P. R. (2012). Sulfide saturation history of the Stillwater Complex, Montana: chemostratigraphic variation in platinum group elements. *Mineralium Deposita* **47**, 151–173.
- Kirkham, R., Dunn, P. A., Kuczewski, A., Siddons, D. P., Dodanwela, R., Moorhead, G., Ryan, C. G., De Geronimo, G., Beuttenmuller, R., Pinelli, D., Pfeffer, M., Davey, P., Jensen, M., Paterson, D., de Jonge, M. D., Kusel, M. & McKinlay, J. (2010). The Maia spectroscopy detector system: engineering for integrated pulse capture, low-latency scanning and real-time processing. *AIP Conference Series* **1234**, 240–243.
- Laurenz, V., Fonseca, R. O. C., Ballhaus, C., Jochum, K. P., Heuser, A. & Sylvester, P. J. (2013). The solubility of palladium and ruthenium in picritic melts: 2. The effect of sulfur. *Geochimica et Cosmochimica Acta* **108**, 172–183.
- Lightfoot, P. C. & Naldrett, A. J. (1983). The geology of the Tabankulu section of the Insizwa Complex, Transkei, southern Africa, with reference to the nickel sulphide potential. *Transactions of the Geological Society of South Africa* **86**, 69–187.
- Lightfoot, P. C., Naldrett, A. J. & Hawkesworth, C. J. (1984). The geology and geochemistry of the Waterfall Gorge Section of the Insizwa Complex with particular reference to the origin of the nickel sulphide deposits. *Economic Geology* **79**, 1857–1879.
- Locmelis, M., Pearson, N. J., Barnes, S. J. & Fiorentini, M. I. (2011). Ruthenium in komatiitic chromite. *Geochimica et Cosmochimica Acta* **75**, 3645–3661.
- Ludwig, K. R. (2009). *Squid 2; A User's Manual*. Berkeley Geochronology Center.
- Maier, W. D. (2004). Monts de Cristal PGE project. Internal Report 2. SouthernEra Resources Ltd, Johannesburg.
- Maier, W. D. (2009). Report on PGE reef potential of the Monts de Cristal PGE project, Gabon. Lonmin Plc, Johannesburg.
- Maier, W. D. & Eales, H. V. (1997). *Correlation within the UG2–Merensky Reef interval of the Western Bushveld Complex, based on geochemical, mineralogical and petrological data*. *Geological Survey of South Africa Bulletin* **120**, 56 pp.
- Maier, W. D., Barnes, S.-J. & Marsh, J. S. (2003). The concentrations of the noble metals in Southern African flood-type basalts and MORB: implications for petrogenesis and sulphide exploration. *Contributions to Mineralogy and Petrology* **146**, 44–61.
- Maier, W. D., Barnes, S. J., Campbell, I. H., Fiorentini, M. L., Peltonen, P., Barnes, S.-J., Smithies, R. H. (2009). Mantle magmas reveal progressive mixing of meteoritic veneer into the early Earth's deep mantle. *Nature* **460**, 620–623.
- Maier, W. D., Barnes, S.-J. & Groves, D. I. (2013). The Bushveld Complex, South Africa: formation of platinum–palladium, chrome- and vanadium-rich layers via hydrodynamic sorting of a mobilized cumulate slurry in a large, relatively slowly cooling, subsiding magma chamber. *Mineralium Deposita* **48**, 1–56.
- Marsh, J. S., Bowen, M. P., Rogers, N. W. & Bowen, T. B. (1989). Volcanic rocks of the Witwatersrand Triad, South Africa, I: Petrogenesis of mafic and felsic rocks of the Dominion Group. *Precambrian Research* **44**, 39–65.
- Marsh, J. S., Bowen, M. P., Rogers, N. W. & Bowen, T. B. (1992). Petrogenesis of Late Archean flood-type basic lavas from the Klipriviersberg group, Ventersdorp Supergroup, South Africa. *Journal of Petrology* **33**, 817–847.
- Martin, H., Smithies, R. H., Rapp, R., Moyen, J.-F. & Champion, O. (2005). An overview of adakite, tonalite–trondhjemite–granodiorite (TTG), and sanukitoid: relationships and some implications for crustal evolution. *Lithos* **79**, 1–24.
- Mavrogenes, J. A. & O'Neill, H. St. C. (1999). The relative effects of pressure, temperature and oxygen fugacity on the solubility of sulfide in mafic magmas. *Geochimica et Cosmochimica Acta* **63**, 1173–1180.
- McDonald, I. & Viljoen, K. S. (2006). Platinum-group element geochemistry of mantle eclogites: a reconnaissance study of xenoliths from the Orapa kimberlite, Botswana. *Transactions of the Institution Mining and Metallurgy* **115**, 81–93.
- McDonough, W. F. & Sun, S.-s. (1995). The composition of the Earth. *Chemical Geology* **120**, 223–253.
- Mungall, J. E. & Brenan, J. M. (2014). Partitioning of platinum-group elements and Au between sulfide liquid and basalt and the origins of mantle–crust fractionation of the chalcophile elements. *Geochimica et Cosmochimica Acta* **125**, 265–289.
- Pagé, P., Barnes, S.-J., Bédard, J. H. & Zientek, M. L. (2012). *In situ* determination of Os, Ir, and Ru in chromites formed from komatiite, tholeiite and boninite magmas: implications for chromite control of Os, Ir and Ru during partial melting and crystal fractionation. *Chemical Geology* **302–303**, 3–15.
- Park, J.-W., Campbell, I. H. & Arculus, R. J. (2013). Platinum-alloy and sulfur saturation in an arc-related basalt to rhyolite suite: Evidence from the Pual Ridge, eastern Manus Basin. *Geochimica et Cosmochimica Acta* **101**, 76–95.
- Paterson, D., de Jonge, M. D., Howard, D. L., Lewis, W., McKinlay, J., Starritt, A., Kusel, M., Ryan, C. G., Kirkham, R., Moorhead, G. & Siddons, D. P. (2011). The X-ray fluorescence microscopy beamline at the Australian Synchrotron. *AIP Conference Proceedings* **1365**, 219–222.
- Patiño Douce, A. E. & Beard, J. S. (1995). Dehydration-melting of biotite gneiss and quartz amphibolite from 3 to 15 kbar. *Journal of Petrology* **36**, 707–738.
- Peck, D. C., Keays, R. R. & Ford, R. J. (1992). Direct crystallization of refractory platinum-group element alloys from boninitic magmas: evidence from western Tasmania. *Australian Journal of Earth Sciences* **39**, 373–387.
- Prendergast, M. (2009). Monts de Cristal Platinum Project, NW Gabon. Geological report on exploration activities. Lonmin plc, Johannesburg.
- Puchtel, I. S. & Humayun, M. (2001). Platinum group element fractionation in a komatiitic basalt lava lake. *Geochimica et Cosmochimica Acta* **65**, 2979–2994.
- Raedeke, L. D. (1982). Petrogenesis of the Stillwater Complex. PhD thesis, University of Washington, Seattle, 212 pp.
- Rehkämper, M., Halliday, A. N., Fitton, J. G., Lee, D.-C., Wieneke, M., & Arndt, N. T. (1999). Ir, Ru, Pt and Pd in basalts and komatiites: New constraints for the geochemical behavior of the platinum group elements in the mantle. *Geochimica et Cosmochimica Acta* **63**, 3915–3934.
- Rollinson, H. R. (2013). *Using Geochemical Data: Evaluation, Presentation, Interpretation*. Routledge.
- Rudnick, R. L. & Fountain, D. M. (1995). Nature and composition of the continental crust: A lower crustal perspective. *Reviews in Geophysics* **33**, 267–309.
- Ryan, C., Kirkham, R., Hough, R., Moorhead, G., Siddons, D., de Jonge, M., Paterson, D., De Geronimo, G., Howard, D. & Cleverley, J. (2010a). Elemental X-ray imaging using the Maia detector array: The benefits and challenges of large solid-angle. *Nuclear Instruments and Methods in Physics Research, Section A* **619**, 37–43.
- Ryan, C., Kirkham, R., Siddons, D., Dunn, P., Laird, J., Kuczewski, A., Moorhead, G., De Geronimo, G., Davey, P.,

- Jensen, M., Paterson, D., de Jonge, M., Howard, D. & Hough, R. (2010b). The Maia 384 detector array in a nuclear microprobe: A platform for high definition PIXE elemental imaging. *Nuclear Instruments and Methods in Physics Research, Section B* **268**, 1899–1902.
- Ryan, C. G. (2000). Quantitative trace element imaging using PIXE and the nuclear microprobe. *International Journal of Imaging Systems and Technology* **11**, 219–230.
- Ryan, C. G., Siddons, D. P., Kirkham, R., Dunn, P. A., Kuczewski, A., Moorhead, G., De Geronimo, G., Paterson, D. J., de Jonge, M. D., Hough, R. M., Lintern, M. J., Hoard, D. L., Kappen, P. & Cleverley, J. (2010c). The new Maia detector system: methods for high definition trace element imaging of natural material. In: Denecke, M. A. & Walker, C. T. (eds) *X-Ray Optics and Microanalysis. AIP Conference Proceedings* **1221**, 9–17.
- Ryan, C. G., Siddons, D. P., Kirkham, R., Li, Z. Y., de Jonge, M. D., Paterson, D. J., Cleverley, J. S., Kuczewski, A., Dunn, P. A., Jensen, M., De Geronimo, G., Howard, D. L., Godel, B., Dyl, K. A., Fisher, L. A., Hough, R. M., Barnes, S. J., Bland, P. A., Moorhead, G. F., James, S. A., Spiers, K. M., Falkenberg, G., Boesenberg, U. & Wellenreuther, G. (2014). The Maia detector array and X-ray fluorescence imaging system: locating rare precious metal phases in complex samples. In: *X-Ray Nanoimaging: Instruments and Methods. Proceedings of SPIE* **8851**, 88510Q.
- Sobolev, S. V., Sobolev, A. V., Kuzmin, D. V., Krivolutsкая, N. A., Petrunin, A. G., Arndt, N. T., Radko, V. A. & Vasiliev, Y. R. (2011). Linking mantle plumes, large igneous provinces and environmental catastrophes. *Nature* **477**, 312–316.
- Sun, S.-s., and McDonough, W. F. (1989). Chemical and isotopic systematics of oceanic basalts: implications for mantle composition and processes, in *Magmatism in the Ocean Basins* edited by Saunders, AD and Norry, MJ: Geological Society Special Publication, **42**, p. 313–345.
- Teigler, B. & Eales, H. V. (1996). *The lower and critical zones of the western limb of the Bushveld Complex, as indicated by the Nooitgedacht boreholes. Geological Survey of South Africa Bulletin* **111**, 126 pp.
- Tomkins, A. G., Rebryna, K. C., Weinberg, R. F. & Schaefer, B. F. (2012). Magmatic sulfide formation by reduction of oxidized arc basalt. *Journal of Petrology* **53**, 1537–1567.
- Toplis, M. J. & Corgne, A. (2002). An experimental study of element partitioning between magnetite, clinopyroxene and iron-bearing silicate liquids with particular emphasis on vanadium. *Contributions to Mineralogy and Petrology* **144**, 22–37.
- Wilson, A. H. (2012). A chill sequence to the Bushveld Complex: insight into the first stage of emplacement and implications for the parental magmas. *Journal of Petrology* **53**, 1123–1168.
- Wingate, M. T. D., Campbell, I. H., Compston, W. & Gibson, G. M. (1998). Ion microprobe U–Pb ages for Neoproterozoic basaltic magmatism in south-central Australia and implications for the breakup of Rodinia. *Precambrian Research* **87**, 135–159.
- Yang, S., Maier, W. D., Lahaye, Y. & O'Brien, H. (2013). Strontium isotope disequilibrium of plagioclase in the Upper Critical Zone of the Bushveld Complex: evidence for mixing of crystal slurries. *Contributions to Mineralogy and Petrology* **166**, 959–974.